Swiss J Geosci (2011) 104:187–210
DOI 10.1007/s00015-011-0070-4

Analysis of tectonic structures and excavation induced fractures in the Opalinus Clay, Mont Terri underground rock laboratory (Switzerland)

Christophe Nussbaum · Paul Bossart · Florian Amann · Charles Aubourg

Received: 31 January 2011 / Accepted: 3 May 2011 / Published online: 21 September 2011

Abstract Excavated in the Opalinus Clay formation, the Mont Terri underground rock laboratory in the Jura Mountains of NW Switzerland is an important international test site for researching argillaceous formations, particularly in the context of deep geological disposal of radioactive waste. The rock laboratory is intersected by naturally formed tectonic structures, as well as artificial fractures primarily formed as a consequence of tunnel excavation and the associated stress redistribution. The description and characterisation of tectonic and artificial structures is, in many cases, of key importance for interpreting the results of the various in situ experiments conducted in the rock laboratory. Systematic small-scale mapping of the tunnel walls and floor, and adjacent niches, provides basic information about the geometry and the kinematics of the geological fractures intersecting the underground laboratory. A compilation of all tectonic structures identified is presented in this paper. The underground laboratory is located in the backlimb of the Mont Terri anticline, a NNW-vergent imbricate fault-bend fold, which is characterised by a pronounced along-strike asymmetry resulting from variously oriented inherited faults. The total shortening accommodated by this structure was estimated by mass (area) balancing to be approximately 2.1 km. The Mont Terri area is significantly affected by N- to NNE-striking normal faults of the Eo-Oligocene Rhine–Bresse transfer zone and by ENE-striking faults of Late Variscan age. Depending on their orientation with respect to the transport direction towards the NNW, these faults served as oblique and frontal ramps during the subsequent Jura thrusting in the Late Miocene. The various fault systems identified in the underground rock laboratory clearly correlate with the regional-scale structures. In addition to classical structural analysis, the anisotropy of magnetic susceptibility was measured to determine the magnetic fabric and strain imprint of the Opalinus Clay. Results indicate a well developed magnetic fabric with a magnetic foliation close to the bedding, and with two distinct magnetic lineations which are probably related to the Mont Terri anticline folding and layer-parallel shortening prior to the folding. Strain imprint is more pronounced in the overturned forelimb, which is consistent with the structural data.

Keywords Jura Mountains · Dogger · Structural geology · EDZ · Magnetic anisotropy · Self-sealing

Editorial handling: A.G. Milnes.

Electronic supplementary material The online version of this article (doi:10.1007/s00015-011-0070-4) contains supplementary material, which is available to authorized users.

C. Nussbaum (✉) · P. Bossart
Federal Office of Topography swisstopo,
Seftigenstrasse 264, 3084 Wabern, Switzerland
e-mail: christophe.nussbaum@swisstopo.ch

F. Amann
Swiss Federal Institute of Technology, Zurich,
Sonneggstrasse 5, 8092 Zurich, Switzerland

C. Aubourg
Laboratoire des Fluides Complexes et leurs Réservoirs,
CNRS, Université de Pau, 6400 Pau, France

1 Introduction

The major aims of the international Mont Terri research project are to investigate and analyse the hydrogeological, geochemical and rock mechanical properties of argillaceous formations, in this case the Opalinus Clay. International research has been ongoing in the Mont Terri underground

rock laboratory since 1996. The Federal Office of Topography (swisstopo) is responsible for the operation of the facility and directs the Mont Terri project. Fourteen organisations from Belgium, Canada, France, Germany, Japan, Spain, Switzerland and the USA, which are all considering clay formations as potential host rocks for deep geological disposal of radioactive waste, are involved in the underground (in situ) experiments. Various other countries worldwide are also investigating claystones as potential repository host rocks.

The Opalinus Clay has been selected in Switzerland as the preferred host rock for disposal of high-level and possibly also low- and intermediate-level radioactive wastes. A Sectoral Plan process, led by the Federal Office of Energy (SFOE), is now underway with the objective of implementing waste disposal at accepted sites. However, the Mont Terri underground rock laboratory is for research purposes only; disposal of radioactive waste in the facility does not come into question. In addition, the tectonic setting and structural geology of the laboratory, as described in this paper (e.g. fracture frequency, fracture sets), is not representative of the potential disposal sites located in the north-eastern part of Switzerland.

The underground rock laboratory lies north of the town of St-Ursanne in Canton Jura (Fig. 1). The research facilities are located at a depth of around 300 m below the Earth's surface and are accessed by the security gallery of the Mont Terri tunnel of the A16 motorway, which passes through the Jura Mountains. The research galleries in the Opalinus Clay layer have a total length of around 500 m.

This paper describes the structural geology of the Opalinus Clay in the Mont Terri underground rock laboratory. All the excavations are documented in detail, particularly in terms of natural and artificial deformation structures. The latter are typically induced by the excavation of galleries and niches in the Opalinus Clay. In Sect. 2, the geological setting of the St-Ursanne region is outlined. The results of the small-scale mapping are presented in Sect. 3. A compilation of all tectonic structures is shown on a structural map of the rock laboratory. Also included in Sect. 3 are the artificial discontinuities developed in the excavation damaged zone (EDZ). In Sect. 4, the observations and data are interpreted and discussed and integrated into the regional-scale tectonic framework. Special emphasis is placed on the geotechnical behaviour and the self-sealing of structures in the EDZ.

2 Geological setting

In the region of St-Ursanne, where the Mont Terri rock laboratory is located, the outcropping sedimentary rocks range in age from Keuper to Quaternary. The presence of the late Palaeozoic clastic sediments is inferred from reflection seismics. They are overlain unconformably by 800 m of Mesozoic limestones, marls and shales, around 400 m of Tertiary Molasse and, locally, Quaternary fluvioglacial sediments. Of special interest is the Dogger unit, which comprises several shallowing-upward regressive cycles, starting with the Aalenian Opalinus Clay and

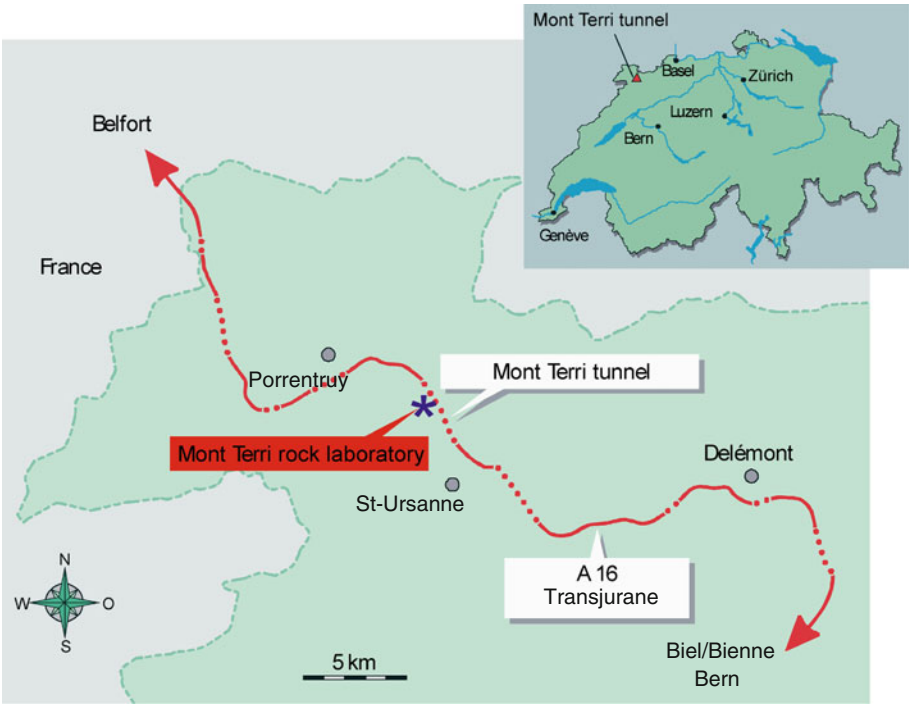

Fig. 1 Location map: the Mont Terri rock laboratory is located in Canton Jura adjacent to the Mont Terri motorway tunnel along the A16 Transjurane connecting Biel to Porrentruy

ending with shallow water carbonates (Blaesi 1987). The Opalinus Clay consists of a monotonous sequence of dark grey, silty, micaceous clays and sandy shales that were deposited around 174 Ma ago. This formation is overlain by a succession of sandy limestones, shales and oolitic ironstones of Early Bajocian age. The overlying middle to upper sequence is distinguished by two facies: the Celtic Platform facies in the north-west (oolitic limestones, "Hauptrogenstein") and the Swabian facies in the south-east, where mudrocks dominate. The boundary between the two facies is located just west of the lower reaches of the Aare River (for location see Fig. 2).

The rock laboratory is located entirely in the Opalinus Clay formation, which has an apparent thickness of 160 m and a true thickness of 90 m. The Opalinus Clay can be divided into five lithostratigraphic sub-units (Blaesi et al. 1991; Schaeren and Norbert 1989; Thury and Bossart 1999; Bossart and Thury 2008), which are grouped into three main facies: (1) a shaly facies in the lower part of the formation (argillaceous and marly shales with micas and nodular, bioturbated layers of marl or with mm-thick layers of sandstones), (2) a sandy facies in the middle and upper part of the formation (marly shales with layers of sandstones and bioturbated lime-stones or with lenses of grey, sandy limestones and mm-thick layers of white sandstones with pyrite) and (3) a thin carbonate-rich, sandy facies in the middle of the formation (calcareous sandstones intercalated with bioturbated limestone beds, the latter showing a high detrital quartz content). The three facies can be explained by varying sedimentary environments in a shallow coastal basin during the time of deposition. The carbonate-rich facies is more abundant in the Franche-Comté Jura region in France and western Switzerland and is almost absent in the Opalinus Clay layers of north-eastern Switzerland. Facies and depositional environments of the Opalinus Clay are described in detail by Blaesi (1987), Burkhalter (1996), Burkhalter et al. (1997) and Allia (1996).

The thickness of the Mesozoic sequence of the Jura belt increases from 1 km in the north (Müller et al. 1984) to some 3 km in the south (Buechi 1965; review in Sommaruga 1997). The sedimentary cover was detached from the basement above the Middle and Upper Triassic evaporites and salt layers of the "Burgundy Trough" (Buxtorf 1907; Burkhard 1990; Jordan 1994; Sommaruga 1999). Deformation was brittle and the temperature of the Middle Jurassic beds never exceeded 100°C (Gehrig et al. 1991). Shortening increases continuously from 0 km at the eastern end of the belt to around 25 km in the central part (Laubscher 1965, 1972; Burkhard 1990; Affolter and Gratier 2004; Philippe et al. 1996).

The regional tectonic formation of the Jura belt and its associated neotectonic activity has already been described by different authors (e.g. Giamboni et al. 2004; Ustaszewski and Schmid 2006). In Middle Miocene times, some 12 Ma ago, the Jura Mountains started to develop (thrusted and folded Molasse sediments: Kälin 1993; Bolliger et al. 1993). The displacement of the frontal Jura fold-and-thrust belt onto the autochthonous foreland did not occur before about 10.5 Ma ago (Becker 2000). The question whether the deformation is still ongoing is unclear. Recent studies (Ustaszewski and Schmid 2006, 2007; Madritsch et al. 2008, 2010) indicate that the deformation is still ongoing, as attested by the Late Pliocene folding of the Réchésy and Florimont anticlines at the junction between the southernmost Upper Rhine Graben and the adjacent Jura front. According to the above authors, the *en échelon* anticlines are associated with thick-skinned reactivation of NNE-SSW- and WSW-ENE-striking faults affecting the basement as wrench faults. Mosar (1999) also postulates this for the current and future evolution of the Alpine foreland. The neotectonic activity is, to some extent, confirmed by the occurrence of earthquakes predominantly in the basement. Focal mechanisms indicate a strike-slip regime with a slight tendency towards extension (Kastrup et al. 2004). More recently, however, the focal mechanism of the Rigney Earthquake (23 February 2004) indicated reverse faulting (compression) in the basement with a focal depth of 10 km and a moment magnitude Mw = 4.5 (Baer et al. 2005). This earthquake probably occurred along an inherited WSW-ENE-striking fault bordering a Permo-Carboniferous graben. These observations collectively suggest that the activity of the belt has not completely ceased but rather continues at a moderate rate. Recently, the current orientation of the maximum horizontal principal stress (SH_{max}) was measured in two deep boreholes (to 5 km depth) of the Enhanced/Engineered Geothermal System, which penetrate granitic basement rocks beneath the city of Basel (Valley and Evans 2009). Available evidence, based on borehole failure analysis (i.e. breakout orientation), suggests that the orientation of SH_{max} above the evaporites is on average N-S and differs from the NW-SE orientation in the basement, as inferred by borehole failure and earthquake data. Further, according to Ustaszewski and Schmid (2007), fault slip data are in agreement with in situ stresses in the cover, suggesting decoupling across the evaporites. Despite this, the corresponding implication in favour of or against ongoing thin-skinned or thick-skinned tectonics is not straightforward.

The internal structure of the Jura Mountains, with its rhomb-shaped synclinal basins and complex interference patterns of cross folds and tear faults, is probably the result of predominantly pre-existing fault systems. These inherited heterogeneities are faults associated with Permo-Carboniferous grabens and the Rhine–Bresse transfer zone, as postulated by many authors (e.g. Laubscher 1970, 1972; Bergerat 1977, 1987; Ziegler 1992; Lacombe et al. 1993;

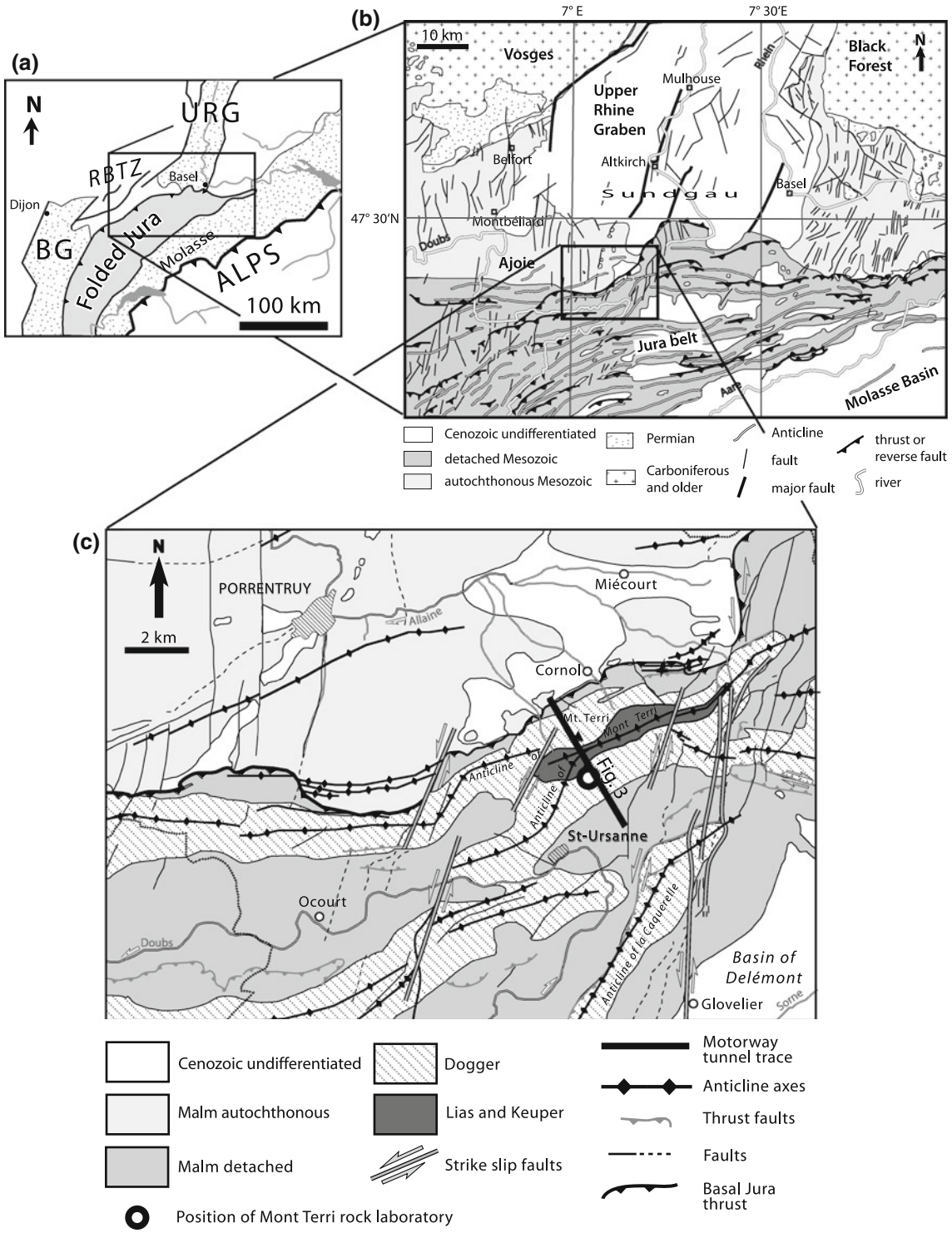

Fig. 2 **a** Tectonic map with the main units of the northern Alpine region. BG Bresse Graben, RBTZ Rhine–Bresse Graben transfer zone, URG Upper Rhine Graben. **b** Large scale tectonic map of the junction between the Jura belt and the Upper Rhine graben. **c** Simplified geological and tectonic map of St-Ursanne (modified after Laubscher 1963). Keuper and Liassic sediments outcrop in the core of the Mont Terri anticline. Note the small rhomb-shaped syncline in the south-western prolongation of the Mont Terri anticline. Its presence may explain the different fault systems identified in the Mont Terri rock laboratory

Laubscher 2001; Ustaszewski and Schmid 2007; Madritsch et al. 2008). The region of St-Ursanne is located in the sinistral transfer zone, which connects the northern end of the Bresse Graben with the southern end of the Rhine Graben (Fig. 2). There is no single major transfer-zone fault, but a rather diffuse transfer zone with both "Rhenish"

(NNE-SSW-striking) and "Permo-Carboniferous" (E-W- and ENE-WSW-striking) faults that were active during the European intra-continental rifting phase in the Paleogene with variable kinematics (Picot et al. 2005; Ustaszewski et al. 2005). During the Jura thrusting phase, the pre-existing faults triggered the development of both frontal and oblique ramps, depending on the fault orientation with respect to the transport direction. Consequently, the Jura fold-and-thrust belt is composed of a series of non-cylindrical anticlines, in which the lateral ends either vanish into so-called transverse or transfer zones (Thomas 1990) or are cut by a conjugate set of sinistral and dextral strike-slip inherited faults, as described by Heim (1919).

The Mont Terri anticline (Fig. 2) developed in this particular structural setting at the junction between the frontal part of the Jura thrust-and-fold belt and the Rhine–Bresse transfer zone. The Mont Terri rock laboratory is located in the south-eastern limb of the Mont Terri anticline, as shown in the cross-section (Fig. 3) from Freivogel and Huggenberger (2003). This cross-section follows the Mont Terri motorway tunnel, which is sub-parallel to the NNW direction of thrusting. The north-western limb of the Mont Terri anticline has been sheared off and thrust over the Tabular Jura. The resulting geometry is an imbricate fault-bend fold, described by Suppe (1983) as the product of passive displacement of the beds above a blind frontal ramp. The entire sedimentary layer-cake structure behaved as a single concordant layer, without being split into duplexes along sedimentary décollement horizons. The Opalinus Clay formation, also named Aalenian Black Shales, served as the major basal décollement level south of the Alemanic terrain in the Helvetic nappe system. In the region of St-Ursanne, there is no indication of the presence of duplexes within the Opalinus Clay (Laubscher 1963; Suter 1981). The overturned forelimb of the Mont Terri anticline is probably related to the steepening of the forward dips by folding of the imbricates (Fig. 3). Assuming that the layer thickness remained constant, this implies that the thrust sheets have undergone additional shear. The total shortening consumed by the Mont Terri anticline was estimated by mass (area) balancing (Freivogel and Huggenberger 2003) to be approximately 2.1 km. The basal décollement level is located in the evaporites of the Muschelkalk formation about 420 m below the lower boundary of the Opalinus Clay formation.

The tectonic map of the St-Ursanne region reveals that the structures are non-cylindrical (Fig. 2). Relatively sharp bends of up to 35° in the regional-scale fold axes control the morphology of this region. Anticlines are segmented and separated from each other by strike-slip faults, mainly oriented N-S and NNE-SSW. These faults are typically associated with subordinate E-W extension, which occurred during the Eo-Oligocene formation of the Rhine–Bresse transfer zone. They were reactivated as sinistral strike-slip faults during the Late Miocene Jura thrusting phase. The ENE-WSW-striking faults are interpreted as left-lateral transform faults connecting the Rhine and Bresse grabens and/or as Miocene extensional faults developed on the forebulge of the European lithosphere as it bends downwards beneath the Alps.

3 Small-scale structural mapping of the rock laboratory

Systematic small-scale mapping of the tunnel walls, floor and adjacent niches provides basic information about the

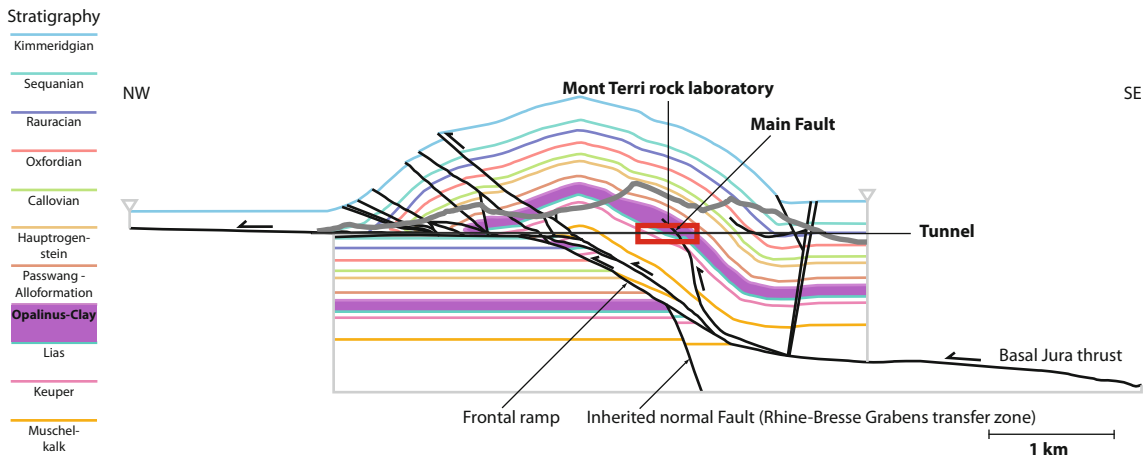

Fig. 3 2D balanced cross-section along the Mont Terri anticline (after Freivogel and Huggenberger 2003). This anticline can be described as a fault-bend fold developed above a frontal ramp and with an overturned forelimb. The location of the rock laboratory is indicated by the *red* rectangle. The Main Fault which outcrops in the rock laboratory is soling in the Jura basal décollement within the Middle Triassic evaporites. Inherited normal faults of the Rhine–Bresse Graben system are overprinted by the Late Miocene Jura deformation

geometry and kinematics of the fractures intersecting the rock laboratory. Tectonic fractures are distinguished from artificial fractures, which are primarily a consequence of tunnel excavation and the associated stress redistribution. The zone around the tunnel where fractures are induced on the micro- and macro-scale is termed the EDZ. Excavated in the backlimb of the Mont Terri anticline, in the rock laboratory the bedding planes dip moderately towards the SSE. Between the lower and upper boundary of the Opalinus Clay formation, dip angles evolve from 30° to 50° (Fig. 4; this figure appears as Electronic Supplementary Material in the online version of the article and can be found as a fold-out at the back of the printed issue).

3.1 The fault systems

In the rock laboratory, the observed tectonic faults can be compiled into three different fault systems (Nussbaum and Bossart 2008): (1) moderately SSE-dipping reverse faults, (2) low angle SW-dipping fault planes and flat-lying (sub-horizontal) faults and (3) moderately to steeply inclined N- to NNE-striking sinistral strike-slip faults. A compilation of the predominant fault planes identified in the rock laboratory is presented in Fig. 4. This structural map shows the faults mapped at the tunnel floor level. The map does not include the fractures induced by tunnel excavation (i.e. EDZ fractures). The orientations of the three fault systems and associated striations are represented on stereoplots. Sealing of the tectonic fractures with calcite slickenfibres and fault gouge minerals is most probably the reason that there is no advective flow in these discontinuities. This also applies for tectonic fault zones such as the "Main Fault" which crosses the motorway tunnel, the security gallery, Gallery 98 and Gallery 08 (Fig. 4).

3.1.1 The SSE-dipping fault system

This fault system is composed mainly of fault planes that are sub-parallel to the bedding planes (Fig. 5a). In the rock laboratory, bedding plane dips range from 30° in the northern part to 50° in the southern part, but the change in dip is not gradual. It occurs abruptly across the SSE-dipping thrust zone called the "Main Fault" (see Sect. 3.2). Slickenside analysis of SSE-dipping faults indicates that the slip direction trends down-dip with a top-to-NNW shear sense. This suggests that slip occurred between the bedding planes during the anticline folding by flexural slip. Most of these fault planes are traceable over entire tunnel faces and sidewalls, suggesting they are of metric scale. Fracture surfaces are either polished (dark) or striated. Shear sense was mainly deduced from striated surfaces formed by preferentially re-oriented clay particles or recrystallised clay and calcite fibres. Polished fractures, which developed as a result of scratching and gouging along the surface, do not provide well constrained shear senses. Nevertheless, it is very likely that slip occurred along these planes.

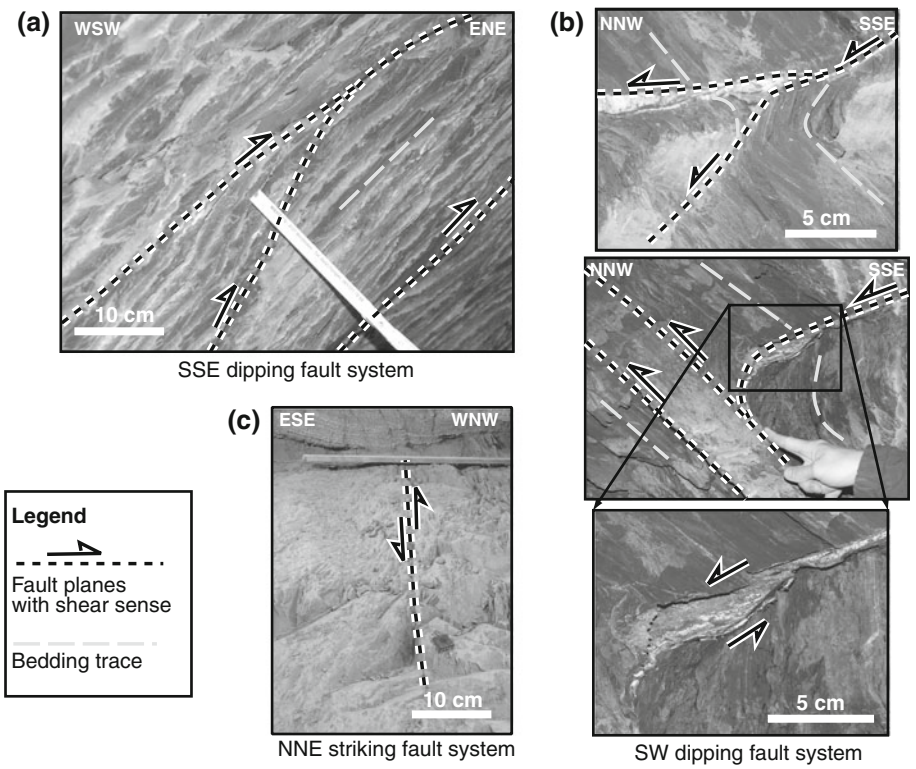

Fig. 5 Photo documentation of the three fault systems identified in the Mont Terri rock laboratory. **a** SSE-dipping faults are sub-parallel to the bedding or cut the layers upwards. **b** SW-dipping faults are characterised by crack-seal accretion structures with *en échelon* geometry indicating shearing towards the NNW. These latter are found to be folded by the SSE-dipping faults. **c** NNE-striking faults are inherited normal faults reactivated in sinistral strike-slip mode

According to small striae lengths observed on striated surfaces, it can be assumed that displacement along these planes was typically limited to the cm-scale. Faults with larger displacements appear on average every 10 m along the tunnel. It was also observed that fault planes are not necessarily parallel to bedding; some are more inclined (with dips up to 70°) and form small ramps through the beds (Fig. 5a). Geometric evidence indicates that displacements along these ramps were limited to the cm-scale. The faults are very heterogeneously distributed along the galleries. Considering all the galleries of the rock laboratory, the frequency ranges from 1 fault per 5 m to 20 faults per metre (Fig. 4).

3.1.2 The low angle SW-dipping and flat-lying fault system

This fault system is composed of two distinct sets: (1) gently SW-dipping fault planes with dip angles ranging from 10° to 40° (20° on average) and (2) flat-lying (sub-horizontal) fault planes with dip angles ranging from 0° to 15° (<10° on average). These two fault systems are considered together due to their similar geometric features. However, as discussed below, their origin is different.

The low angle SW-dipping faults show extents on the meter to several decametre scale. Fracture planes are mainly striated with slickenfibres and sometimes stepped. Occasionally, two distinct striations were measured on the SW-dipping fault planes: (1) down-dip to the SW and (2) sub-horizontal NW-trending (Fig. 4). The shear sense indicates normal faulting for the SW-dipping striation and thrusting movement towards the NNW for the second striation set. Crosscutting criteria indicate that the SW-trending lineation is overprinted by the NNW-directed striation. This latter striation consists of groove marks and fibrous steps which overgrow the SW-dipping striation. However, sometimes only one striation was observed on SW-dipping fractures. In such cases, the shear sense was systematically towards the NNW. Lithological markers in the clay matrix, such as sandy layers and/or oxidised layers bearing siderite, showed offset due to these thrust faults in the range of 2–5 cm. These fault planes were very often associated with a 1–4 cm thick, white, coarse mineralisation acting as crack seals. The crack-seal accretion structures consist of idiomorphic celestite, calcite and dolomite (Burkhard, personal communication). These crack-seal accretion structures were observed to be locally folded or cut by the SSE-dipping fault planes (Fig. 5b). Folded veins are sheared off and exhibit *en échelon* geometry, indicating a thrusting displacement towards the NNW.

The sub-horizontal faults clearly branch from bedding-parallel SSE-dipping faults (Fig. 6). Although they branch from SSE-dipping faults, they strike E-W, dipping slightly to the south. The fault plane extent ranges from metric to decametric scale. Sub-horizontal fracture planes are mainly striated and stepped. In some cases, stepped fractures are partially polished. Flat-lying fault planes are also associated with mm-scale calcite veins.

3.1.3 The N- to NNE-striking fault system

N- to NNE-striking fault planes were identified at various locations in the rock laboratory (Fig. 4). N-S-striking fault planes dip moderately with angles varying between 20° and 60° (on average 45°) mainly to the east, while NNE-striking faults are steeply inclined and dip generally towards the WNW (Fig. 5c). For NNE-striking faults, slickenside analyses suggest an oblique slip direction composed of sinistral shear movements, possibly related to a transpressive regime. Bedding planes are drag-folded in the vicinity of NNE-striking faults. N-S-striking faults bear down-dip slickensides, indicating normal faulting. The extent of this fault system is metric to decametric scale. These faults are arranged in two north-trending alignments on the scale of the rock laboratory (Fig. 4). The first fault zone is located in the northern part and dips to the east, while the second dips to the west. The Main Fault is located between the two.

Besides the three fault systems described in the previous sections, two significant E-W-striking reverse faults dipping towards the south at a high angle (70°) were identified in Gallery 08. These fault planes are characterised by down-dip striation produced by scratching and gouging, and show a top-to-N sense of shear.

3.2 Structural characterisation of the "Main Fault"

The largest tectonic structure outcropping in the rock laboratory is a 0.8–3 m-thick fault zone called the "Main Fault" (Fig. 4). In the following, the architecture of the Main Fault will be described with reference to the two intersections which have been studied in detail, the fault intersection in Gallery 98 (Fig. 7) and that in Gallery 08 (Fig. 8). This SSE-dipping fault zone is more inclined than the bedding planes but dips towards the same direction (N150°). The angular difference between the fault zone boundaries and the bedding planes is, on average, 15°. The internal structure of the Main Fault is very heterogeneous, comprising zones with fault gouge, C′-type shear bands as defined by Passchier and Trouw (1996), meso-scale folds, microfolds, numerous fault planes and apparently undisturbed parts. The zone is a thrust or reverse fault zone, with shear movement top-to-NNW as suggested by kinematic indicators. The thickness of the thrust zone varies laterally; in Gallery 08 it is approximately 3 m thick, while in Gallery 98, at a lateral distance of about 50 m from Gallery 08,

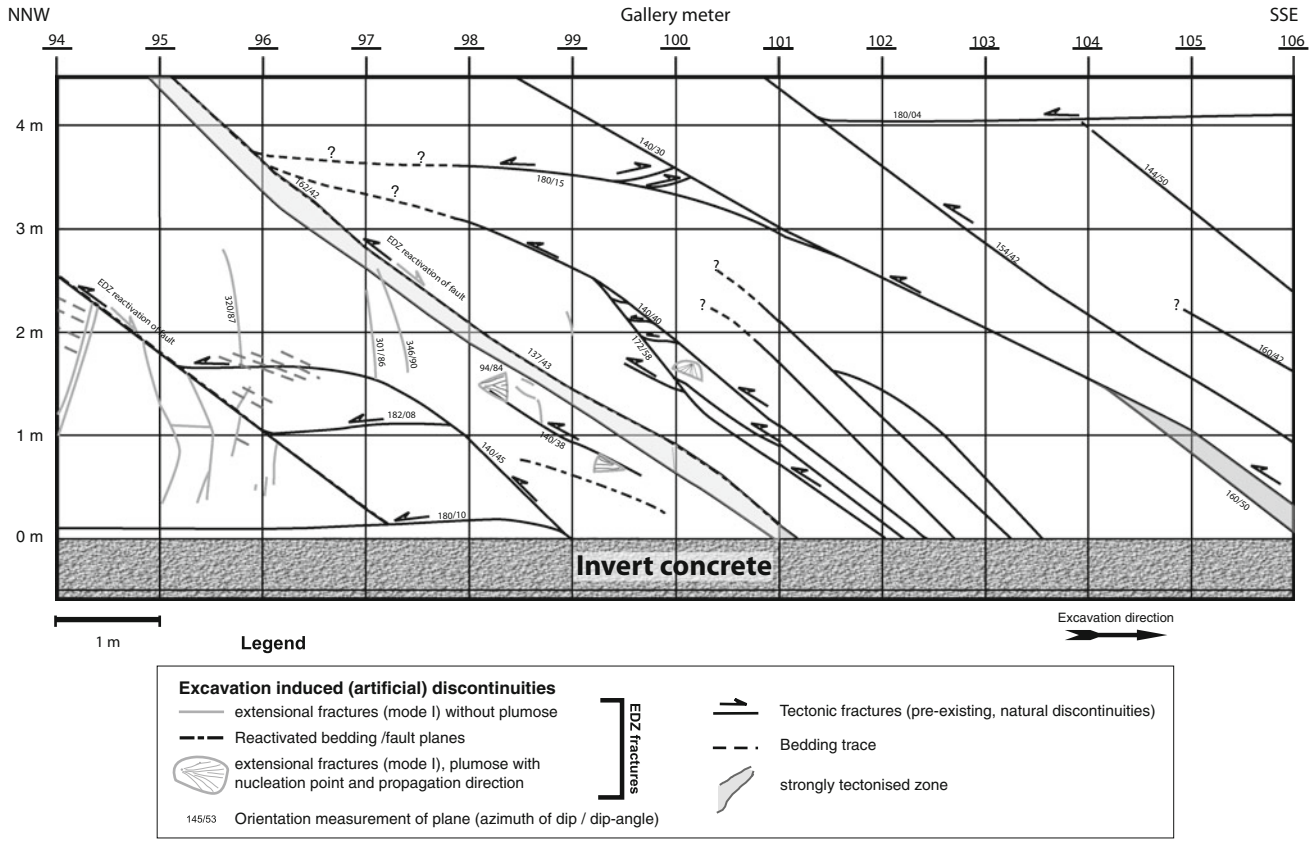

Fig. 6 Small-scale mapping of the eastern sidewall of Gallery 08 between gallery metre GM94 and GM106. For location refer to Fig. 4. South-dipping, sub-planar faults developed from moderately SSE-dipping fault planes. The whole system is activated in thrusting mode. The SSE-dipping strongly tectonised zone was reactivated in normal faulting during the excavation phase

the thickness is 1 m. In addition, the lower and upper fault boundaries dip to the SSE with 50° and 55° in Gallery 98 and with 40° and 45° in Gallery 08, respectively. Thus, the Main Fault seems to flatten and also to curve towards the SW (Fig. 4). Small-scale mapping of these outcrops provides valuable information on the structure and lateral variability of the Main Fault. A detailed structural description of the Main Fault is presented in the following sections for Galleries 98 and 08, respectively.

When compiling the different fault systems throughout the rock laboratory, it becomes obvious that the Main Fault separates certain structures into two different parts. Sub-horizontal fault planes are found mainly in the footwall of the Main Fault (northern part of the rock laboratory), while SW-dipping faults are mapped mainly in the hanging wall (southern part of the rock laboratory) with some scarce occurrences in the footwall. Adding to this observation, it should be noted that the frequency of bedding-parallel, SSE dipping fault planes is significantly larger in the hanging wall where the fault frequency is up to 20 faults per metre in some tunnel sections. This is in contrast to the footwall, where the fault frequency is <1 fault per 5 m.

3.2.1 Main Fault in Gallery 98

The Main Fault outcropping in Gallery 98 is approximately 1 m thick (Fig. 7). The lower and upper fault boundaries dip on average with 55°–60° to the SSE. The bedding planes in the footwall are less inclined (range 30–35°) than those in the hanging wall (range 42°–46°). The inner structure of the Main Fault was investigated by small-scale mapping of the outcrop in Gallery 98 and core analysis from boreholes crossing the Main Fault. It is characterised by penetrative ductile structures expressed by C′-type shear bands (also called extensional crenulation cleavage) as illustrated in Fig. 7a. Alternatively, the insert in Fig. 7b shows a duplex, i.e. an entirely fault-bounded domain within the shear zone, bounded by a floor and a roof thrust

Fig. 7 Small-scale mapping of the Main Fault intersected in Gallery 98. For location refer to Fig. 4. The Main Fault is a SSE-dipping fault zone which is more inclined than the bedding planes but dips with the same strike (150°). The angular difference between the fault zone boundaries and the bedding planes is 15° on average. **a** View of the western sidewall. **b** View of the eastern sidewall. The inner structure is characterised by C′-type shear bands. **c** Paleostress analysis indicates NNW-SSE shortening

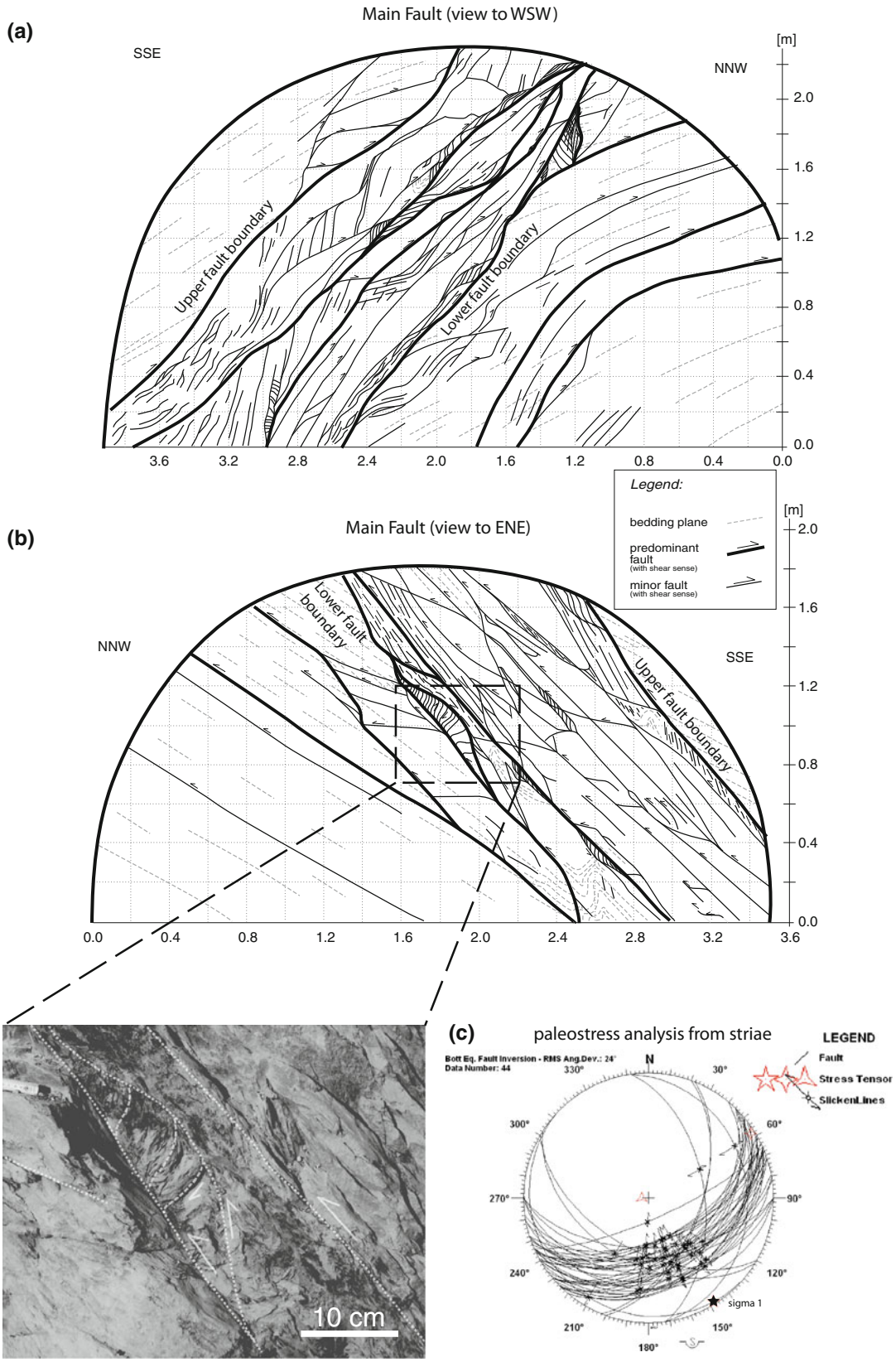
(a)
Main Fault (view to WSW)
SSE
NNW
[m]
2.0
1.6
1.2
0.8
0.4
0.0
Upper fault boundary
Lower fault boundary
3.6
3.2
2.8
2.4
2.0
1.6
1.2
0.8
0.4
0.0
Legend:
bedding plane
predominant fault (with shear sense)
minor fault (with shear sense)
(b)
Main Fault (view to ENE)
NNW
SSE
Lower fault boundary
Upper fault boundary
0.0
0.4
0.8
1.2
1.6
2.0
2.4
2.8
3.2
3.6
10 cm
(c)
paleostress analysis from striae
LEGEND
Fault
Stress Tensor
SlickenLines
Bott Eq. Fault Inversion - RMS Ang.Dev.: 24°
Data Number: 44
N
30°
60°
90°
120°
150°
180°
210°
240°
270°
300°
330°
sigma 1

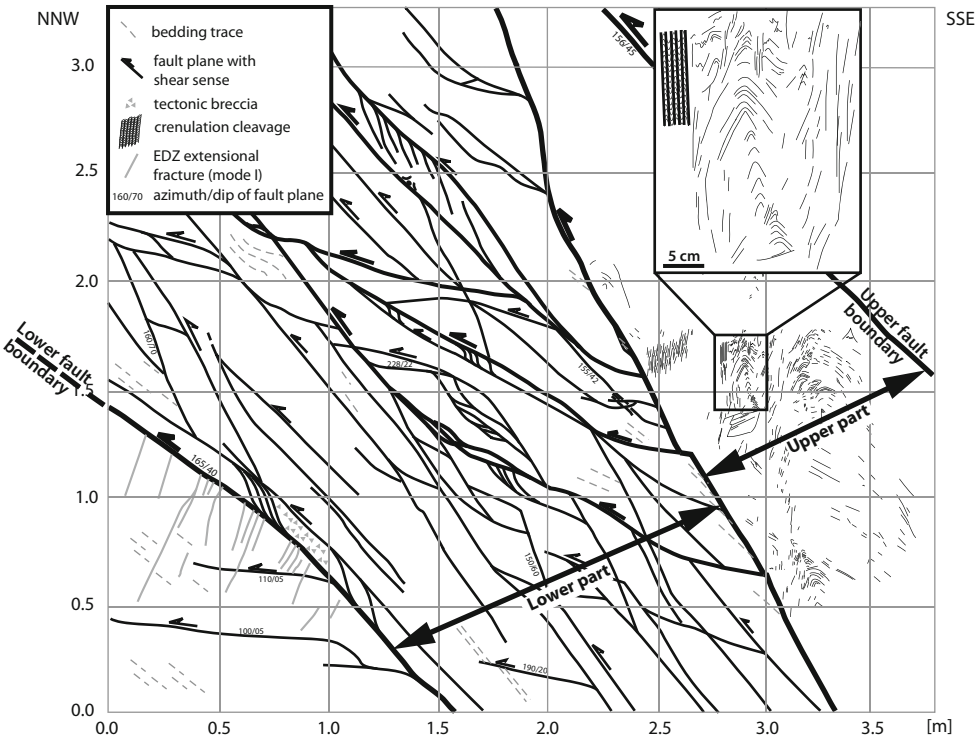

Fig. 8 Small-scale mapping of the Main Fault intersected in Gallery 08. For location refer to Fig. 4. The Main Fault intersecting Gallery 08 is a 3 m thick thrust zone with a complex internal geometry characterised by two distinct structural domains separated by a reverse fault dipping steeply to the SSE. The *upper part* is strongly deformed and folded and has locally developed a crenulation cleavage. The *lower part* is characterised by apparently undisturbed rock masses embedded by a succession of fault planes and localised C′-type shear bands associated with NW thrusting displacement. The lower boundary fault is partly formed by tectonic breccia

and in which bed rotation may also be common. The internal structure of the Main Fault is heterogeneous and is composed of apparently undisturbed blocks embedded in strongly tectonised parts composed of centimetric to decimetric-thick shear zones and fault gouges of fine, dark rock powder. Kinematic indicators suggest that the Main Fault is a thrust zone with a shear displacement top-to-NNW. Based on fault-slickenside pair analysis and applying the fault inversion method, the derived paleostress tensor of the Main Fault indicates that sigma 1 is oriented sub-horizontal along an axis 330°–150° (Fig. 7c).

3.2.2 Main Fault in Gallery 08

The Main Fault intersecting Gallery 08 is a 3 m-thick thrust zone with a complex internal geometry (Fig. 8). The lower and upper fault boundaries dip with 40° and 45° to the SSE, respectively. The beds in the hanging wall and footwall dip less than the shear zone boundary. The upper fault boundary is truncated by a sub-horizontal fault in thrusting mode, showing an offset of 3 cm towards the NNW. The internal structure of the Main Fault is characterised by two distinct structural domains separated by a reverse fault dipping at high angle to the SSE (mean dip 70°). This fault strikes sub-parallel to the lower and upper fault boundaries of the Main Fault. The upper part is strongly deformed and folded and shows close similarities to crenulation cleavage geometry as described by Passchier and Trouw (1996). These mm-scale structures can be distinguished with the naked eye; they consist of a sub-vertical spaced cleavage with smooth cleavage domains. Adjacent to this spaced cleavage, there are domains with mm- to cm-scale fold hinges. Axial planes within the Main Fault and close to the upper thrust plane of the Main Fault are folded. In contrast, the lower part is characterised by apparently undisturbed rock blocks embedded in a series of fault planes and localised C′-type shear bands associated with NNW thrusting displacement. A tectonic breccia borders the lower boundary fault. This observation contrasts with the ductile penetrative structures identified in the upper part of the Main Fault.

3.3 Excavation damaged zone

3.3.1 Relation of EDZ to tectonic structures

According to Bossart et al. (2002, 2004), the fracture network related to tunnel excavation can be subdivided into an inner and outer shell. The inner shell, with an average extent of 1 m from the tunnel circumference, is typically characterised by extensional fractures sub-parallel to the tunnel wall and smaller-scale shear fractures. These fractures developed mainly in the tunnel walls (sidewall, ceiling, floor) and tunnel faces. Extensional fractures are often linked by smaller-scale shear fractures, resulting in an interconnected fracture network. The presence of gypsum spots on the fracture planes in the inner shell is probably related to pyrite oxidation (Bossart et al. 2002) as a result

of air circulation coming from the tunnel. Therefore, the fracture network is most probably connected to the tunnel. The outer shell, between 1 m and around 2 m from the tunnel circumference, is composed of individual extensional fractures that are not, or only partially, interconnected.

The small-scale mapping of the EZ-B niche provides an illustrative example of the EDZ fracture network around Gallery 04 (Fig. 9). Three different sets of EDZ fractures were identified behind the sidewall: (1) extensional fractures parallel to the Gallery 04 sidewall, (2) oblique striking extensional fractures with respect to the Gallery 04 axis and (3) reactivated bedding planes in the vicinity of the tunnel wall. A detailed analysis of the EDZ fracture development around the EZ-B niche can be found in Yong (2007) and Yong et al. (2010). The extent and size of these extensional fractures is limited to the metric scale. Detailed mapping of the tunnel floor revealed metric-scale sub-horizontal extensional fractures. These fracture surfaces are characterised by a plumose structure with ripple structures and well developed fringe zones (e.g. *en échelon* or hackle structures; Bahat 1986) indicating the fracture nucleation point and the propagation direction (Fig. 10). No evidence of slip can be observed along these rough fracture surfaces which develop exclusively in tensile mode, most probably as a consequence of unloading of the tunnel floor (Bossart et al. 2002). It should be noted that similar plumose structures were also often found on vertical extensional fracture planes developed parallel to the sidewall and tunnel face.

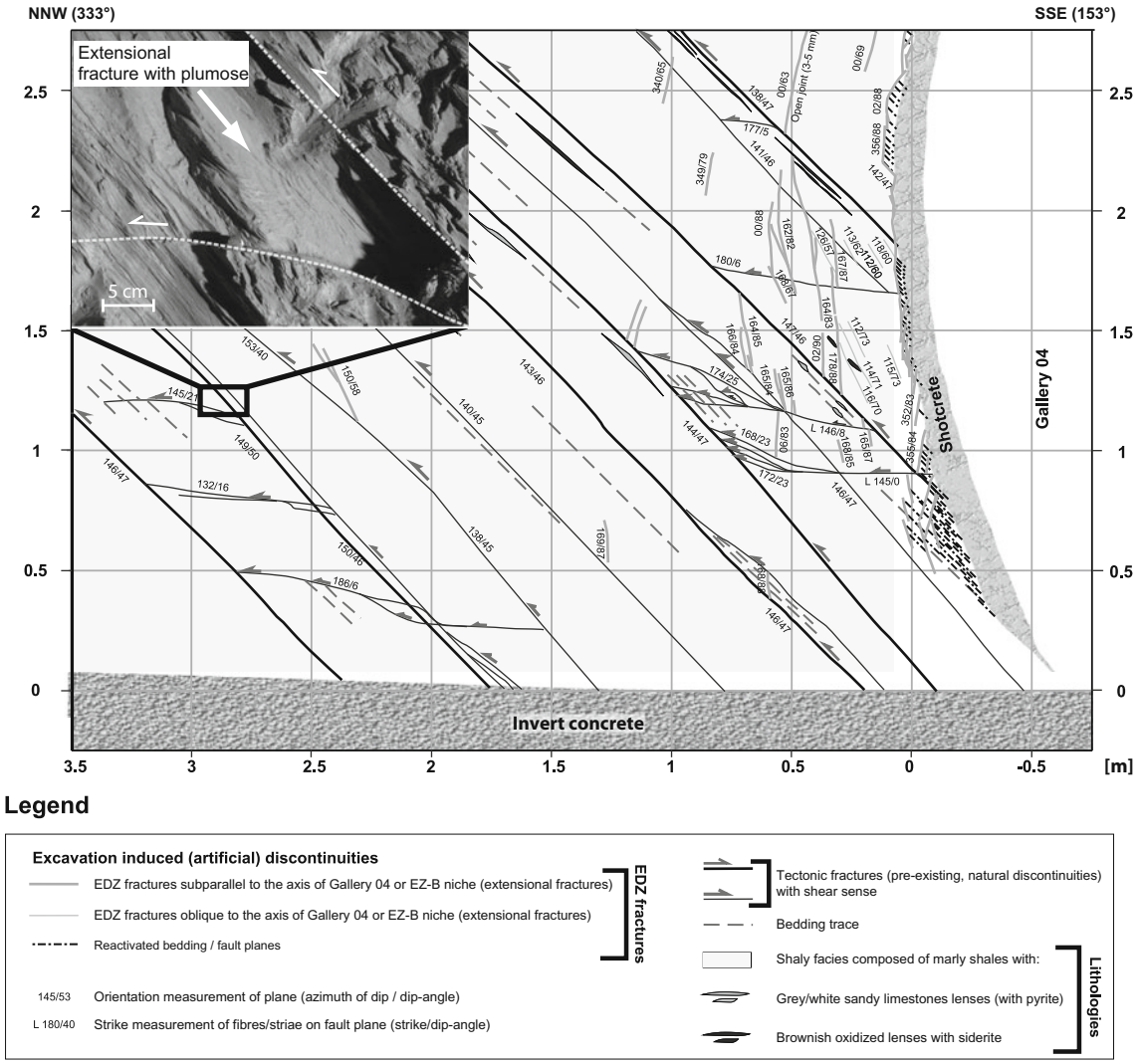

Fig. 9 Small-scale mapping of the eastern sidewall of the EZ-B niche. For location refer to Fig. 4. This vertical cross-section provides an illustrative example of the EDZ fracture network, which developed around Gallery 04. Three different sets of EDZ fractures were identified behind the sidewall: (1) extensional fractures parallel to Gallery 04, (2) oblique striking extensional fractures with respect to the Gallery 04 axis and (3) reactivated bedding planes in the vicinity of the tunnel wall. A detailed analysis of the EDZ fracture development around the EZ-B niche can be found in Yong et al. (2010)

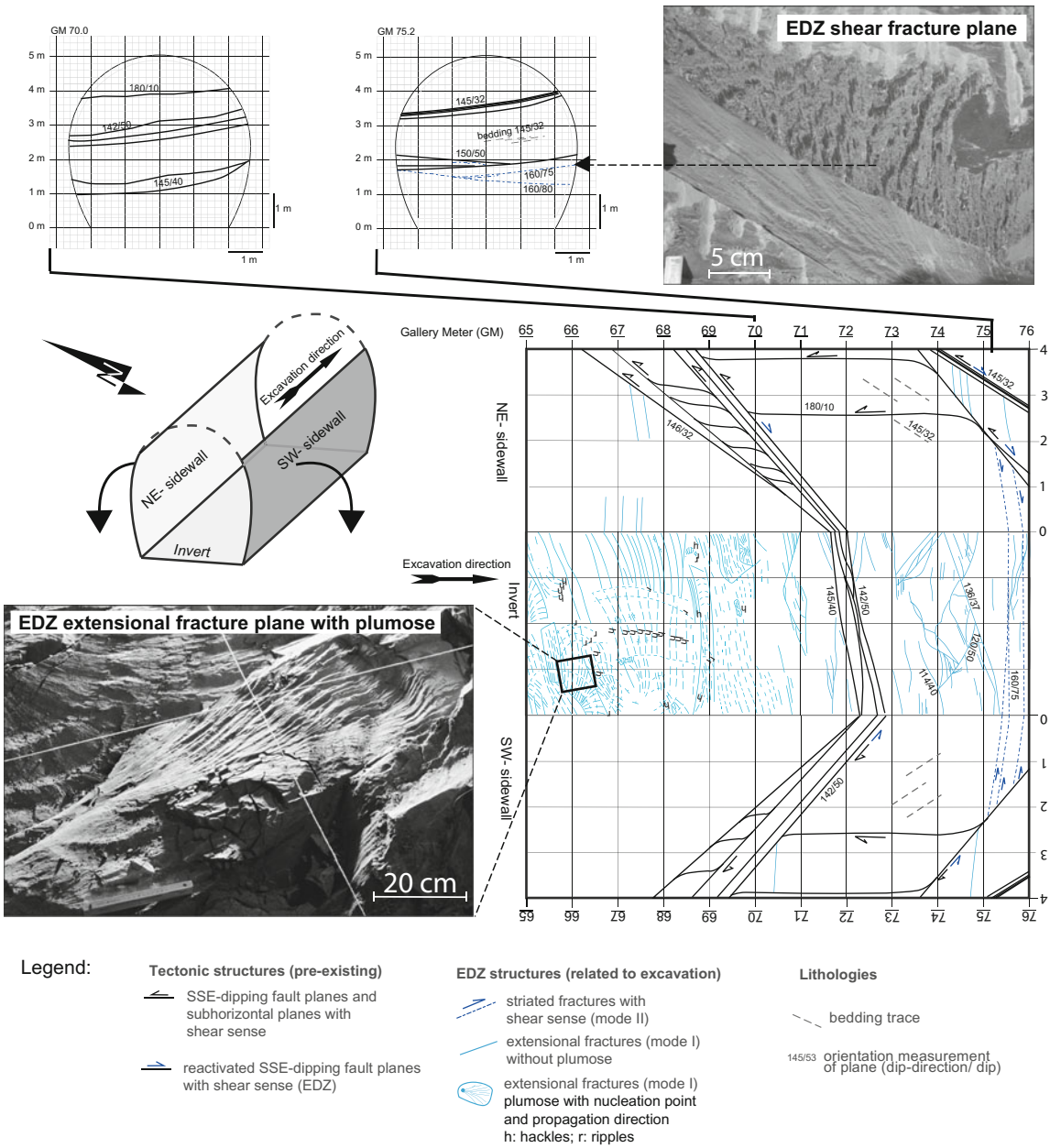

Fig. 10 Detailed mapping of the tunnel floor and sidewall in Gallery 08 between gallery metre GM 65 and GM 76. For location refer to Fig. 4. The mapping revealed metric-scale, sub-horizontal extensional fractures on the tunnel floor. These fracture surfaces are characterised by a plumose structure with ripple structures and well developed fringe zones (e.g. *en échelon* or hackle structures) indicating the fracture nucleation point and the propagation direction. Mainly observed on tunnel face, ceiling and sidewall, certain striated fracture planes are not of tectonic origin. Parts of them are associated with other excavation-induced fractures. They dip with angles ranging from 40° to 80° and are systematically more inclined than the bedding planes. These excavation-induced shear planes are associated with down-dip striation indicating normal displacement along the fracture plane

Detailed mapping during the excavation of the 100 m long straight section of Gallery 08, which is oriented perpendicular to the bedding strike, provided new insights into the formation of EDZ fractures. Gallery 08 was excavated from north-west to south-east, sub-parallel to the bedding plane dip. Over a section of 30 m of Gallery 08, shotcrete was not applied continuously and the development of EDZ fractures could be observed as the distance to the face increased. The mapping of Gallery 08 revealed that certain striated fracture planes are not of tectonic origin. Parts of them are associated with other excavation-induced fractures. These EDZ shear fractures were observed in tunnel faces, ceiling and sidewall. Their extent ranges from 1 to 5 m or even larger. Individual fractures intersected the

whole front of Gallery 08. These shear fractures have the same strike as the bedding planes, but dip more steeply (Fig. 10). The bedding plane dip in Gallery 08 ranges from 30° to 45° southwards. EDZ shear fractures dip with angles ranging from 40° to 80° and are systematically more inclined than the bedding planes. The difference in dip angle ranges between 20° and 40°. These excavation-induced shear planes are associated with down-dip striation, indicating normal displacement along the fracture plane. In contrast to tectonic faults which are typically characterised by dark polished surfaces with striation, EDZ shear fractures bear poorly developed striations possibly formed by preferentially re-oriented clay particles (Fig. 10). Recrystallised clay or slickenfibres have not been observed so far on excavation-induced shear fracture surfaces.

It was also observed that extensional EDZ fractures often do not propagate through pre-existing natural discontinuities such as well developed inclined bedding planes and/or fault planes. The systematic mapping of the galleries showed that the spatial distribution of EDZ fractures is, to a certain extent, controlled by pre-existing faults. Figure 11 illustrates the geometric relationship between a low angle thrust plane and extensional EDZ fractures. This example shows that EDZ fractures are limited to the rock mass below the fault plane, which was most probably reactivated as a normal fault during the excavation phase. Within a period 24 h after excavation, a relative shear displacement of approximately 2 cm was observed.

Numerous related observations were made, such as the set of extensional EDZ fractures which formed below the lower boundary fault of the Main Fault (Fig. 8). Whatever their orientation, pre-existing faults spatially limited the propagation of EDZ fractures into the adjacent rock mass. In tunnel sections where only a few pre-existing faults were identified, the majority of EDZ fractures was Mode I (extensional) and the EDZ fracture network was better developed. Slip along pre-existing small-scale fault planes and bedding planes is also found in the EDZ fracture network. As a consequence of the above-mentioned rock mass heterogeneities (e.g. frequency of pre-existing fractures and fault zones) and their influence on stress redistribution, the EDZ is heterogeneous in both the mode and possibly the depth of fracturing.

As a conclusion, the EDZ fracture network is composed of: (1) extensional fractures (Mode I) often associated with plumose structures. These fractures are sub-parallel to the gallery sidewalls or front walls, (2) excavation-induced shear fractures (Mode II) with the same strike as the bedding planes but dipping at a higher angle and (3) reactivated bedding and fault planes.

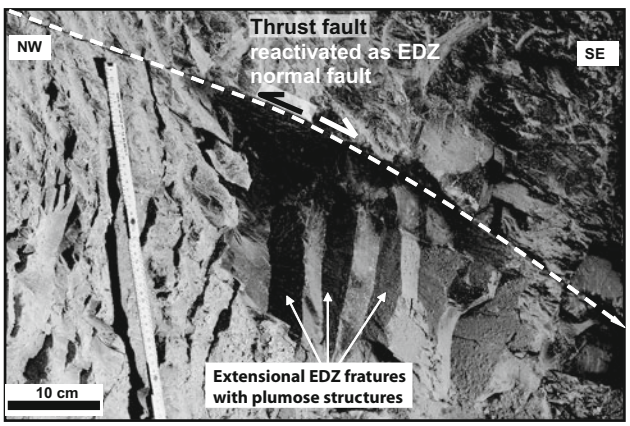

Fig. 11 Geometric relationships between a pre-existing fault and fractures induced by the excavation phase. The thrust fault limits the sub-vertical extensional EDZ fractures upwards. During the excavation phase, the thrust plane was reactivated as a normal fault (Photo: © Comet Photoshopping GmbH, Zürich)

3.3.2 Self-sealing of the EDZ fractures

Long-term hydrotesting was carried out in EDZ fractures at various locations in the Mont Terri rock laboratory (Bossart et al. 2004). The aim of the experiments was to analyse whether the relatively high fracture transmissivity decreases with time when exposed to free water, indicating self-closure of the network due to swelling processes. This process is called self-sealing. One of these test sequences was carried out on the tunnel wall at tunnel metre 84.5 in Gallery 98 (for location see Fig. 4). The tunnel section contains one injection and 15 observation boreholes, each about 1 m in length, crossing the EDZ fracture network (Fig. 12a). The sequence started with pneumatic testing under unsaturated conditions, followed by artificial saturation of the EDZ fracture network and carrying out constant head and constant rate injection tests. The transmissivity estimates from a total of 9 hydrotests performed after the pneumatic tests over a period of more than 2 years resulted in a continuously decreasing transmissivity trend for each subsequent test (Fig. 12b). The relatively large spread of transmissivity for tests 1 and 2 is probably due to non-linear processes shortly after the initial saturation. The results of Fig. 12 show clearly that the transmissivity decreased from an initial value of 4×10^{-7} to 2×10^{-9} m^2/s after 777 days. The decreasing transmissivity trend still continues, suggesting that self-sealing is still going on.

The conclusion of this long-term hydrotesting at various locations confirms the self-sealing of EDZ fractures. Fracture transmissivities decreased by two orders of magnitude over a period of 2 years and this trend is still ongoing. The final transmissivity after completion of self-sealing is not known, but is expected to be in the same order as that of the

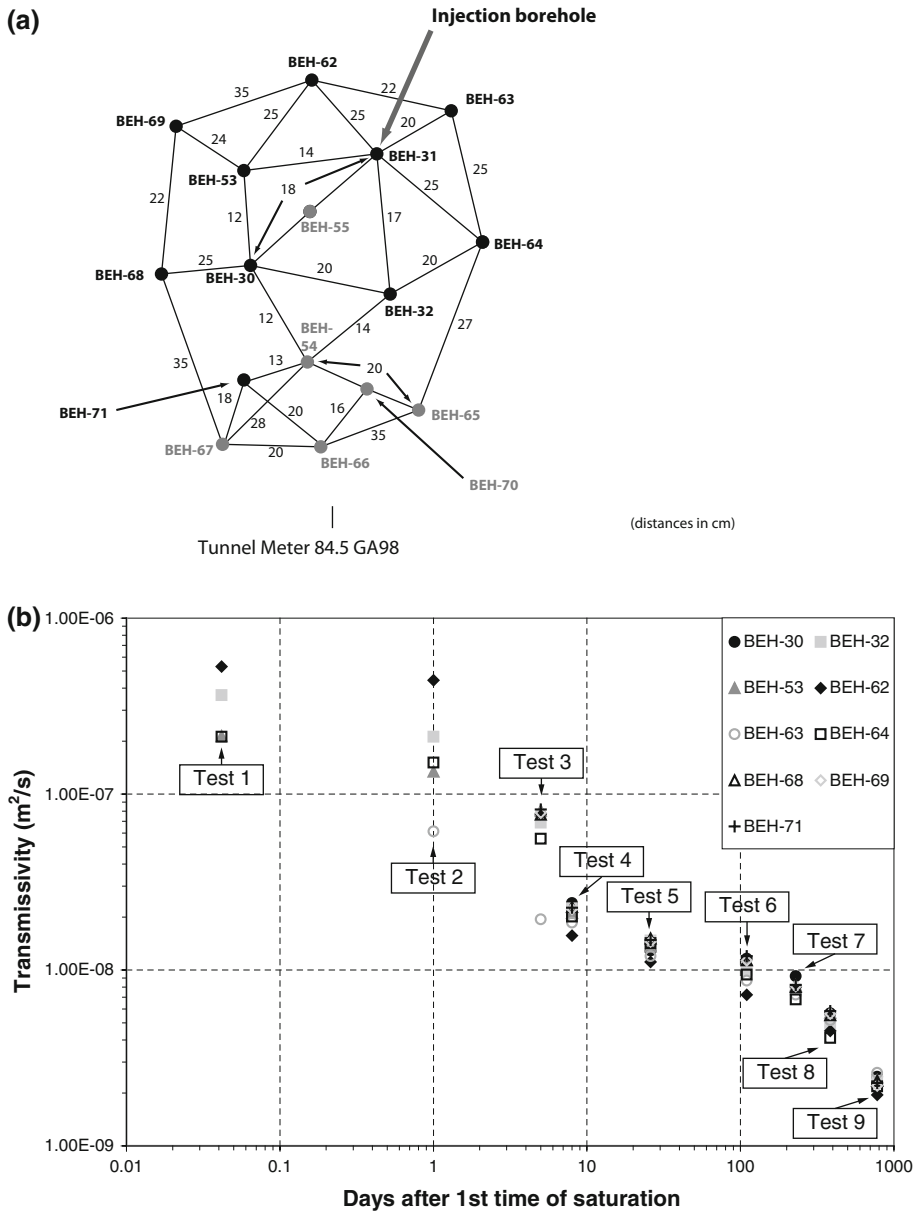

Fig. 12 **a** Schematic borehole mouth configuration at the tunnel wall in Gallery 98, gallery metre GM 84.5. The length of each of the 16 boreholes is around 1 m. The *numbers* between two boreholes indicate the distance between the corresponding test intervals in cm. **b** Log-plot of calculated transmissivity (m^2/s) versus time, derived after each of the nine hydraulic tests. The *negative trend* shows that the transmissivity in the EDZ fracture network decreases by about two orders of magnitude over a period of 2 years. This reduction in transmissivity is due to swelling processes with subsequent reduction of the fracture widths, which is termed self-sealing of EDZ fractures

undisturbed Opalinus Clay, which varies between 10^{-14} and 10^{-12} m^2/s if the test interval is 1 m long.

3.4 Anisotropy of magnetic susceptibility data

3.4.1 Methodology

The anisotropy of magnetic susceptibility (AMS) was measured on a series of Opalinus Clay samples taken from the fore- and backlimb of the Mont Terri anticline and from the Triassic dolomites in the core of the anticline. This sampling strategy aims to compare the magnetic fabric along three locations in the Mont Terri anticline; the backlimb, the hinge and the forelimb. In terms of strain imprint, only the magnetic fabric of the forelimb and the backlimb can be compared because it is carried by homogeneous Opalinus Clay. Measurements were performed to determine the anisotropy of low-field magnetic susceptibility of 10.8 cc cores (diameter 25 mm; length 22 mm). AMS allows the detection of both the shape orientation of ferromagnetic minerals and the crystal orientation of clays (Borradaile 1988; Hrouda 1982; Rochette et al. 1992). The AMS measurement is a non-destructive method which gathers the contribution of billions of minerals within the 10.8 cc of the core. Generally, sedimentary rock types allow reliable AMS measurements, which provide a measure of the magnetic foliation, magnetic lineation and scalar parameters, which can be related to strain (Hirt et al.

1988). The magnetic foliation is marked by the planar preferred orientation of magnetic minerals. It is generally parallel to bedding. There are, however, exceptions where a slaty cleavage has developed. The initial magnetic foliation is then gradually overprinted by a new magnetic foliation, parallel to the cleavage (Borradaile and Jackson 2004). The magnetic lineation is generally parallel to a structural lineation, such as the bedding/cleavage intersection or stretching. Interestingly, a magnetic lineation is also frequently observed in weakly deformed rocks where no visible counterpart is detected.

The magnetic anisotropy of each magnetic mineral is approximated by a 3×3 symmetric tensor. The overall AMS representative for a 10.8 cc sample is determined as the average of billions of individual tensors. The AMS tensor is typically represented by an ellipsoid with $K1 > K2 > K3$ axes. The K3 axis represents the pole of magnetic foliation and the K1 axis the magnetic lineation. AMS data are processed using bootstrap statistics from Constable and Tauxe (1990). From a random picking of AMS data, hundreds of mean tensors are obtained. The mean of all tensors is then calculated, providing a mean pole of magnetic foliation and a mean magnetic lineation. From the magnitude of these axes, three classical anisotropy parameters can be computed: the mean susceptibility (Km), the percentage of anisotropy (P%) and the shape parameter (T). The mean susceptibility provides an indication of the content of magnetic minerals. It typically ranges from 100 to 300 μSI in claystones, but it can have negative value (~ -10 μSI) in carbonates. This suggest that the AMS in claystone is primarily controlled by clays and ferromagnetic minerals, while the AMS in carbonate is controlled by calcite (which is diamagnetic $Km < 0$). In sediments, P% generally ranges from 0.1 (threshold of AMS measurement) to 5. This suggests that the shape of the ellipsoid is weakly anisotropic and is mostly spherical. This weak anisotropy is often forgotten as there is generally excellent grouping of AMS data in sedimentary rock. The analyses of the above-mentioned parameters (Km, P%) provide a reliable estimate of the preferred orientation averaged over billions of grains. The shape parameter T of AMS provides an indication of the strain ellipsoid. When $0 < T < 1$, the shape is oblate (disc-shaped) and when $T < 0$ the shape is prolate (cigar-shaped).

In a fold-and-thrust belt such as the Jura belt, the response of sedimentary rocks depends on the burial depth, strain and rock type. In addition, the folding process provides the record of additional strain. For instance, Aubourg et al. (2004) showed the difference in strain records between some detachment-like (less strain) and ramp-like (more strain) anticlines. Burial imposes the formation of a magnetic foliation parallel to the bedding. During layer-parallel shortening or folding, it is possible to observe the progressive loss of bedding-related magnetic foliation. At this stage, the poles of individual magnetic foliation carried by the samples generally draw a girdle that develops parallel to the strain plane, including the strain shortening direction. When strain increases, a tectonic magnetic foliation can develop, without necessarily its textural counterpart on field inspection (spaced cleavage or stylolite). This early magnetic cleavage has been detected in numerous cases, but appears to develop preferentially in carbonates and clastic rocks (Frizon de Lamotte et al. 2002; Robion et al. 2007). The T parameter visualises the loss-and-formation of magnetic foliation. Generally, buried sediments have $T > 0$. In the event that a new magnetic foliation develops, T decreases and can even reach negative values (prolate shape of AMS). Although promising, the agreement between P% and strain is not straightforward in sedimentary rocks as it depends strongly on the magnetic mineralogy (Borradaile and Mothersill 1984).

3.4.2 Results from the rock laboratory

Results from samples taken in the rock laboratory and its surroundings indicate that the Opalinus Clay displays a well defined magnetic foliation which is related to bedding (Fig. 13). This result is expected in claystones where cleavage is absent. Results also indicate a linear preferred orientation within the magnetic foliation. In the backlimb of the anticline, the magnetic foliation lies within the bedding planes (Fig. 13d). The magnetic lineation shows two groups, a western one (trend 215°; plunge 27°) that is slightly more anisotropic and a second one with a subhorizontal E-W-trending magnetic lineation. However, the magnetic lineation is poorly defined (Fig. 13d). It should be noted that this SW-plunging magnetic lineation is also observed in the forelimb, where the magnetic foliation is also related to the bedding (here overturned) (Fig. 13b). The magnetic lineation in this context is better expressed and lies within the SW quadrant (trend 201°; plunge 35°). The magnetic susceptibility does not show any clear trend between forelimb and backlimb. This indicates that the magnetic mineralogy is essentially similar. Aubourg et al. (2008) showed that the magnetic susceptibility is equally carried by paramagnetic clays and stoichiometric magnetite. The shape of the AMS ellipsoid is oblate in both limbs for the Opalinus Clay, but the degree of anisotropy is different. The AMS of Opalinus Clay from the forelimb is significantly more anisotropic and less oblate ($T = 0.85 \pm 0.12$; $P\% = 6.7 \pm 1.2$) than in the backlimb ($T = 0.70 \pm 0.24$; $P\% = 4.6 \pm 0.4$). The similarities in magnetic mineralogy of the Opalinus Clay in both limbs imply that the strain imprint is more pronounced within the overturned forelimb.

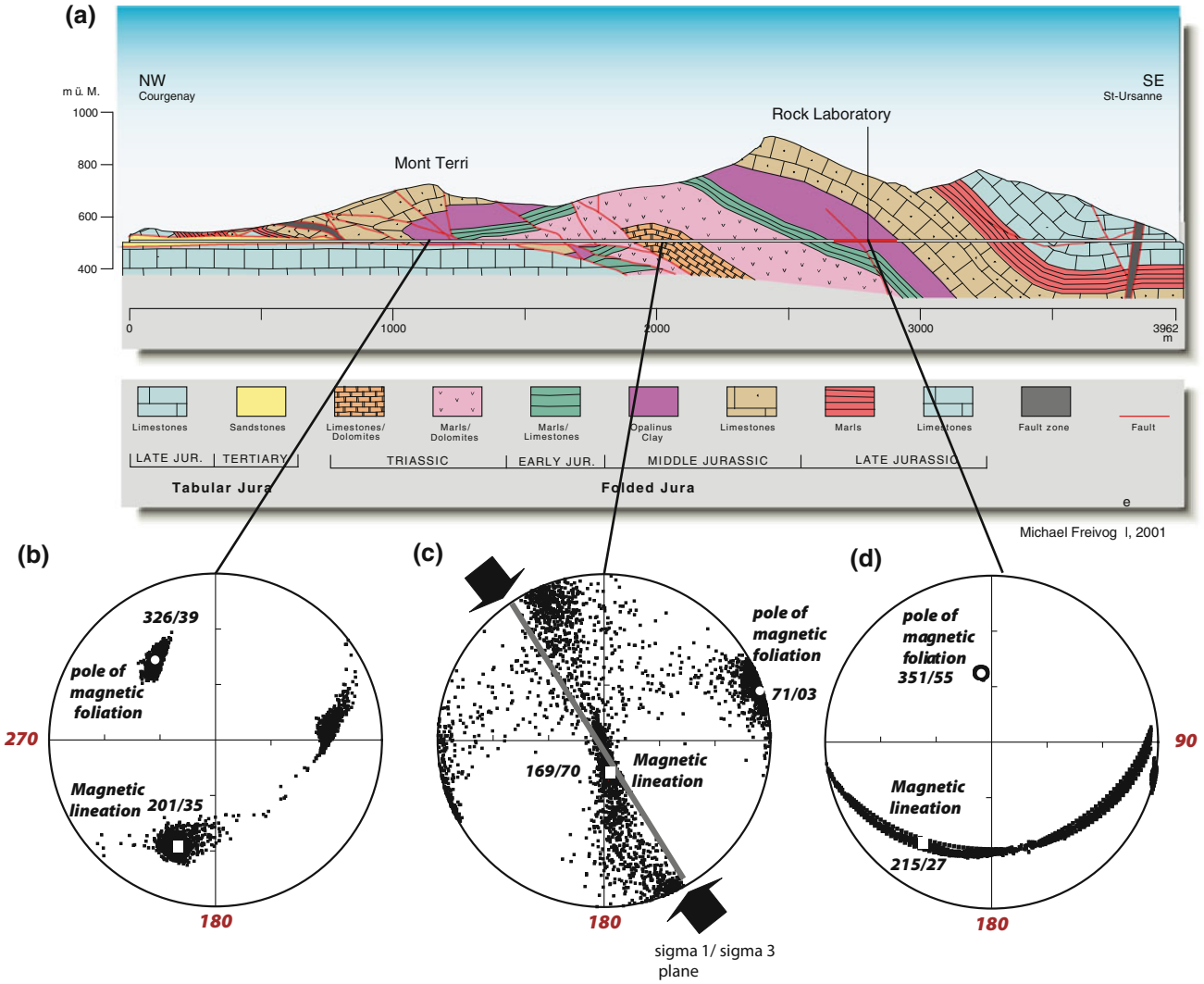

Fig. 13 Anisotropy of magnetic susceptibility results processed using bootstrap statistics for the geometry of the Mont Terri anticline. **a** Cross-section from Freivogel and Huggenberger (2003). The magnetic foliation of the Opalinus Clay is parallel to the bedding (**b**, **d**), while the magnetic foliation of Triassic carbonates generally trends parallel to the NNW-SSE shortening direction (**c**)

As the facies of Triassic carbonates is markedly different from the Opalinus Clay, their magnetic mineralogy cannot be compared, and hence nor can the shape of AMS. The magnetic fabric of Triassic carbonates taken from the anticline hinge shows interesting features. At first glance, the magnetic fabric seems to be scattered (Fig. 13c), but it is in fact a composition of two end-members: one foliation is parallel to the bedding as found for the Opalinus Clay and the other is perpendicular to the bedding. The bootstrap statistics emphasise the two trends. This fabric differs from the fabric in the Opalinus Clay, where magnetic foliation is parallel to bedding. It should be noted that the trend of the vertical magnetic lineation (trend 169°; plunge 70°) is parallel to the principal stress axes sigma1–sigma3 of the paleostress, which was derived from paleostress indicators such as faults and striae within the Main Fault (Fig. 7c).

4 Interpretation and discussion

4.1 Relationships of fault systems with regional-scale structures

The SSE-dipping fault planes are formed mainly as a consequence of bedding-parallel slip related to the folding of the Mont Terri anticline. This structure is an imbricate fault-bend-fold, probably a result of passive displacement of beds above a blind frontal ramp at depth (Fig. 3). The forelimb is overturned, which indicates that additional shearing occurred. On the basis of cross-section mass balance considerations, the core of the fault-bend fold is affected by a small imbrication (Fig. 3). This latter was not detached along the Opalinus Clay horizon but propagated upwards through the sedimentary layers. The entire

sedimentary succession was displaced as a single unit and no significant internal detachment occurred within the Opalinus Clay. This is in contrast with the Aalenian black shales of the Helvetic nappes, which acted as the main detachment level, probably due to the absence of evaporites in these regions.

The SW-dipping faults are folded or cut by the SSE-dipping faults. This suggests that bedding-parallel slip induced folding of these SW-dipping fault planes, which are often associated with crack-seal accretion structures (e.g. veins) (Ramsay and Huber 1983; Passchier and Trouw 1996). Furthermore, *en échelon* structures with a shear sense top-to-NNW indicate that these folded veins had been sheared off beforehand. This suggests that, prior to being folded or offset by the SSE-dipping faults, these veins were reactivated in thrusting mode. It should be recalled that two distinct striations are measured on SW-dipping fault planes: down-dip to the SW and sub-horizontal NW-directed. Crosscutting criteria indicate that the SW-trending striation associated with normal displacement is older than sub-horizontal NW-trending striation. Crack-seal accretion structures probably developed during the normal faulting phase. Development of moderately dipping normal faults can possibly be related to a SW-NE lateral extension in response to the displacement of the beds above the frontal ramp towards the NNW. As shown on the schematic block diagram (Fig. 14), the fold axis of the Mont Terri anticline diverges into two segments towards the SW. In fact, a small rhomb-shaped "syncline" replaces the Mont Terri anticline axis in its southwest prolongation. This rhomb-shaped basin is bordered by anticlines trending NNE-SSW and NE-SW. Anticlines are assumed to be related to NNW vergent thrusts. Relatively sharp bends of up to 35° in the trend of map-scale fold axes give rise to a rhomb-shaped basin which has some similarities with the Val-de-Ruz basin (Tschanz and Sommaruga 1993). NE-SW-trending anticlines probably formed as cylindrical folds. NNE-SSW-trending anticlines are assumed to be non-cylindrical. This is interpreted as folding above frontal and oblique ramps, respectively, with an overall transport direction to the NNW. Oblique ramps formed above inherited NNE-striking faults related to the Rhine–Bresse transfer zone, leading to a "wrench fold" type anticline. The NNE-trending anticline "La Caquerelle" further south is also interpreted as folding above a regional-scale oblique ramp triggered by a "Rhenish" fault (Fig. 2). These NNE faults were also identified in the rock laboratory. Kinematic criteria indicate that they were reactivated in sinistral

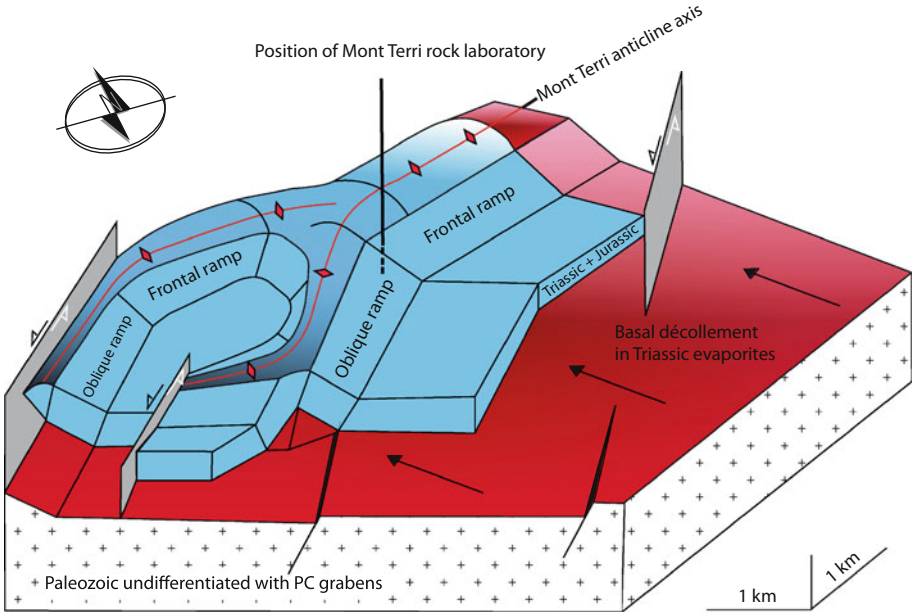

Fig. 14 3D simplified block diagram of the Mont Terri anticline and the surrounding structural features. *Black arrows* indicate the transport direction towards the NNW along the basal décollement plane depicted in *red*. The Mont Terri anticline is explained by fault-bend folding above a frontal ramp. SW-dipping normal faults are interpreted as being concomitant with lateral extension towards the SW during folding. This is explained by the doming structure plunging towards the SW due to the rhomb-shaped syncline acting like a "lateral ramp". This is not a true lateral ramp but a combination between frontal and oblique ramps resulting in a "lateral" ramp geometry. The rhomb-shaped basin is bordered by anticlines trending NNE-SSW and NE-SW, formed as non-cylindrical and cylindrical folds, respectively. These structures were interpreted as folding above frontal and oblique ramps, respectively, with an overall transport direction to the NNW. Inherited NNE-striking faults related to the Rhine–Bresse graben system are reactivated in sinistral strike-slip mode

strike-slip mode. These data are compatible with the fault-slip analyses performed at the surface along the Caquerelle anticline as well as further north along-strike (Ustaszewski and Schmid 2006).

In Gallery 08, two ENE-WSW-striking high angle reverse faults dipping southwards were identified. These reverse faults can be interpreted as relicts of inverted normal faults developed on the forebulge of the European lithosphere that was bent downwards beneath the Alps (Burkhard and Sommaruga 1998; Valley et al. 2004) during the Oligo-Miocene extensional phase (Laubscher 1987; Homberg et al. 1994). This latter is corroborated by the deposition of gompholites, which are angular calcareous breccia deposited in lake environments (Favre et al. 1937; Duringer 1988; Berger 1996; Picot et al. 2005). Alternatively, these two ENE-WSW-striking normal faults could be also interpreted as left-lateral transform faults connecting the Rhine and Bresse grabens.

4.2 Interpretation of the Main Fault

The Main Fault can be considered as a shear zone along which thrusting to the NNW occurred. It is assumed to be a minor splay soling in the Jura basal décollement within the Middle Triassic evaporites. As there is no evidence of this fault at the surface, it probably ends on the top of the Opalinus Clay formation. A first look would favour an interpretation of the Main Fault as a fault-propagation fold as defined by Suppe and Medwedeff (1990). This may be corroborated by the slight increase in thickness of the Opalinus Clay outcropping along the security gallery (along-tunnel thickness of 160 m instead of 135 m as expected considering a mean dip angle of 40° for beds and a true thickness of the Opalinus Clay of 90 m). Nevertheless, a fault-propagation fold would imply that the shortening is compensated by folding beyond the frontal fault tip, which is not supported by any evidences. The cross-section in Fig. 3 shows that the Main Fault ends without transferring any shortening into folding. Furthermore the beds of the hanging wall dip less than the fault ramp, which is in this case the shear zone boundary (55°). The angular difference of beds between the footwall (30°–35°) and the hanging wall (40°–45°) ranges from 10° to 15°. These latter values correspond to the true backlimb dip and a ramp dip of 20°–25° after unfolding to the footwall bedding dip. These geometric relationships favour an interpretation as a shear fault-bend fold (Suppe et al. 2004), in contrast with a classical fault-propagation fold or fault-bend fold where backlimb dips are parallel to the fault ramp. The thickening mapped in the Opalinus Clay intersecting the rock laboratory could be also explained by a pure-shear fault-bend fold, where the layers are commonly shortened and thickened above the ramp. However since the available outcrops along the Main Fault are limited due to the gallery height, it is not possible to obtain all necessary details to distinguish between the two end-members: simple-shear or pure-shear fault-bend fold. The current steep dip of the Main Fault (on average 55°) suggests that it was possibly initiated at an early stage of the Mont Terri anticline history (as shown in the balanced cross-section in Fig. 3), before the folding of the anticline occurred. Thrust ramps commonly develop with dips between 20° and 30°. Thus, the Main Fault was probably passively steepened during the folding of the Mont Terri anticline, which formed as a hanging wall anticline during the *in sequence* transport of the detached sedimentary succession on top of the frontal ramp (dip angle of 30°) located further to the northwest. The imbrication within the fault-bend fold contributed to further steepening of the Main Fault. Thus, the current steep dip of the Main Fault may be explained by both the tilting of the early shear fault-bend fold and by the subsequent folding caused by the imbrication within the fault-bend fold.

The internal structure of the Main Fault provides additional information on the kinematics. The steep fault observed in the Main Fault outcropping in Gallery 08 may be interpreted as an inherited structure which produced intense folding and crenulation cleavage. In the event that an older planar fabric is present in the rock mass, such as the bedding planes in the present case, the associated mechanical anisotropy may give rise to a harmonic, regularly spaced folding which produces crenulation cleavage. Such geometry typically occurs when shearing is involved in the deformation processes. Microfolds observed in microlithons could be relicts of the folded bedding planes during the first deformation stage which is related to the layer-parallel shortening. Development of spaced cleavage probably occurred later during the ongoing shear deformation and especially during the tilting of the Main Fault as result of the fault-bend folding. C′-type shear bands are also interpreted as being formed later when the Main Fault was already tilted and the shear bands were ideally oriented with an angle of 45° with respect to the direction of the maximum principal stress. C′-type shear bands may nucleate at locations of high differential stress. Thus, it is likely that stress and strain were heterogeneously distributed within the Main Fault during the folding of the Mont Terri anticline. In short, the hanging wall accommodated more strain that the footwall, which is in line with the characteristics of shear fault-bend folds. Sub-horizontal faults are typically found close to the Main Fault and especially in the footwall; these are interpreted as being related to the late contraction of the Mont Terri anticline (see below).

It should be noted that this ductile deformation took place under very low temperature but probably under a

high shear component. According to Mazurek et al. (2006), the maximum temperature during Cretaceous burial reached 85°C in the Mont Terri Opalinus Clay. The temperature then decreased and the maximum temperature during Miocene burial did not exceed 55°C. This means that the temperature during the development of the Main Fault was probably not higher than 55°C. Nevertheless, a crenulation cleavage developed. These issues will be considered in more detail through additional microstructural studies planned for the near future.

4.3 Interpretation of AMS data

Results from samples taken in the rock laboratory and its surroundings indicate that the magnetic foliation is well developed in the Opalinus Clay. In the backlimb of the anticline, a single magnetic foliation is, on average, subparallel to the bedding. The magnetic lineation shows two separate clusters: the first plunges towards the SW and the second has a sub-horizontal E-W-trending magnetic lineation. In the overturned forelimb, the magnetic lineation is well defined and plunges towards the SW.

The SW-plunging magnetic lineation is interpreted as having formed contemporaneously with the Mont Terri anticline since its orientation is parallel to the fold axis. The plunging to the SW may be explained by the divergence of the anticline axis into two segments towards the SW and the related rhomb-shaped basin. In contrast, the horizontal E-W-trending magnetic lineation, only recorded in the backlimb, is probably related to the layer-parallel shortening that took place in an earlier stage of the folding of the Mont Terri anticline. Alternatively, the origin of the E-W magnetic lineation could also be older than the Late Miocene Jura folding phase. In fact, based on fault slip analysis and stylolites throughout the Jura belt, various authors suggest two different deformation phases with different shortening directions: N-S and NW-SE (Plessmann 1972; Tschanz 1990). The N-S shortening is interpreted as being related to the Eocene Rhine–Bresse graben system. Records from this older deformation phase are measurable in areas not affected by Jura folding. According to AMS data, strain imprint is more pronounced in the forelimb than in the backlimb of the fold. This could explain the absence of the older E-W-trending magnetic lineation in the overturned forelimb where the lineation was probably completely overprinted due to the intense shear deformation. Whatever the age of the E-W magnetic lineation, its preservation in the backlimb is consistent with strain data derived from AMS data.

The magnetic fabric of Triassic dolomites from the hinge of the anticline is a composition of two end-members: one foliation parallel to bedding as observed in the Opalinus Clay and another normal to bedding. The trend of the vertical magnetic lineation is parallel to the principal sigma1–sigma3 axis of the paleostress derived from brittle analysis of the Main Fault. For this reason, the development of the vertical magnetic lineation in Triassic dolomites is interpreted to be contemporaneous with the paleostress recorded in the Main Fault. One approach for explaining the mechanism of this process is the opening of Mode 1 extensional fractures and subsequent infilling with iron oxides. The observation of bitumen in the dolomite core corroborates this hypothesis. Fluid migration close to the hinge of the Mont Terri anticline is vertical.

4.4 Structural evolution

The three fault systems identified in the Mont Terri rock laboratory are illustrated in Fig. 14 as a simplified block diagram integrating the surrounding map-scale structures. Based on fault crosscutting considerations and kinematics criteria, the implications of the different fault systems are discussed and the following deformation sequence for the Mont Terri area can be suggested:

1. Development of N- to NNE-striking normal faults. This fault system is interpreted as part of the inherited structures related to Eo-Oligocene formation of the European rift system (i.e. Rhine–Bresse transfer zone).
2. Initiation of the Main Fault as a shear fault-bend fold in the early stage of the Late Miocene Jura thrusting. The presence of a steeply inclined inherited fault, as identified in the Gallery 08, might be the reason of the nucleation of the shear fault-bend fold at that location. Nevertheless, the development of this structure was aborted since it didn't reach the surface. The deformation propagates further towards NW along the basal thrust in the Triassic evaporites.
3. Folding of the Mont Terri anticline as a fault-bend fold above a frontal ramp, located north-west of the Main Fault. This assumes that deformation occurred *in sequence* as a result of the propagation of the Alpine foreland towards the NNW according to the "distant push" or "Fernschub" theory in the sense of Laubscher (1961). Synchronously with the folding above the frontal ramp, lateral normal faulting occurred towards the SW with crack-seal accretion structures. SW-dipping normal faults are interpreted as a result of the doming structure plunging towards the SW due to the rhomb-shaped "syncline" acting like a "lateral ramp". This is not a true lateral ramp but a combination between frontal and oblique ramps resulting in a "lateral" ramp geometry. The observation that SW-

dipping normal faults are mainly concentrated in the hanging wall of the Main Fault (i.e. topographically higher) supports this interpretation. Together with the displacement of the beds above the ramp, the Main Fault is also passively tilted in the hanging wall of the Mont Terri anticline. The current steep dip of the Main Fault results from this tilting.

4. Ongoing deformation and related increasing shear triggered the reactivation of SW-dipping normal faults in thrusting mode. Related kinematics indicates thrusting towards the NNW.
5. Late contraction of the Mont Terri anticline produced flexural bedding-parallel slip. Reverse SSE-dipping faults developed parallel to the bedding and propagated northwards through sub-horizontal splays dipping slightly towards the south. In the same stage, SW-dipping faults were folded or cut by bedding-parallel faults. The geometry and kinematics of sub-horizontal faults suggest N-S shortening rather than the transport direction towards the NNW, which prevailed previously. This slight orientation change may be tentatively explained by considering the regional-scale structures. The Mont Terri area is located entirely in the southern prolongation of the Eo-Oligocene Ferrette half graben (Ustaszewski and Schmid 2006) whose master faults delineated the Mont Terri anticline westwards and eastwards. The detached sediments above the Middle Triassic evaporites may have experienced a slight clockwise rotation as a result of the reactivation in sinistral strike-slip mode of the NNE-striking faults bordering the Mont Terri anticline (Fig. 14). A gentle clockwise rotation of the detached sediments was also postulated by Ustaszewski and Schmid (2006) to explain the pronounced along-strike asymmetries of the Ferrette anticline further north. Based on paleomagnetic data, Gehrig et al. (1991) also found that detached sediments had undergone clockwise rotation of about 10° between inherited NNE-trending oblique ramps. Another structural argument may corroborate this scenario. The Mont Terri anticline is an imbricate fault-bend fold with an overturned forelimb as depicted in Fig. 3. The presence of an overturned forelimb may imply that non-parallel folding occurred due to imbricate fault-bend folding with a high fundamental cut-off angle. This may suggest that a slight rotation occurred during the ongoing deformation.

According to the deformation sequence proposed above, it should be noted that both fault systems associated with veins are interpreted as being the expression of the earliest phase (SW-dipping faults) and the latest phase (sub-horizontal faults) of the Jura thrusting phase.

4.5 Conceptual model of the EDZ fracture network

A conceptual model of the EDZ fracture network was already proposed by Bossart et al. (2002, 2004). The fracture network can be subdivided into an inner and outer shell (Fig. 15). The inner shell (f1 = 1 m) typically consists of an interconnected and air-filled fracture network where extensional fractures are linked by meso-scale shear fractures. This shell is characterised by enhanced transmissivity (values varying between 1×10^{5} and 1×10^{-9} m^2/s). The highest transmissivity was found in the first 40 cm of the tunnel wall. The outer shell, which is limited to a zone f2 = 2 m around the tunnel, consists of partially water-saturated, isolated extensional fractures which exhibit a much smaller transmissivity (values varying between 1×10^{9} and 1×10^{12} m^2/s). The three-dimensional arrangement of the EDZ fractures in both the inner and outer shell is influenced by the pronounced bedding plane anisotropy, especially at the bottom and top of the gallery. Oxidation phenomena such as gypsum spots on fracture surfaces were observed only in the inner zone. The orientation of certain extensional fractures on the sidewall of Gallery 08 (Fig. 11) suggests that these

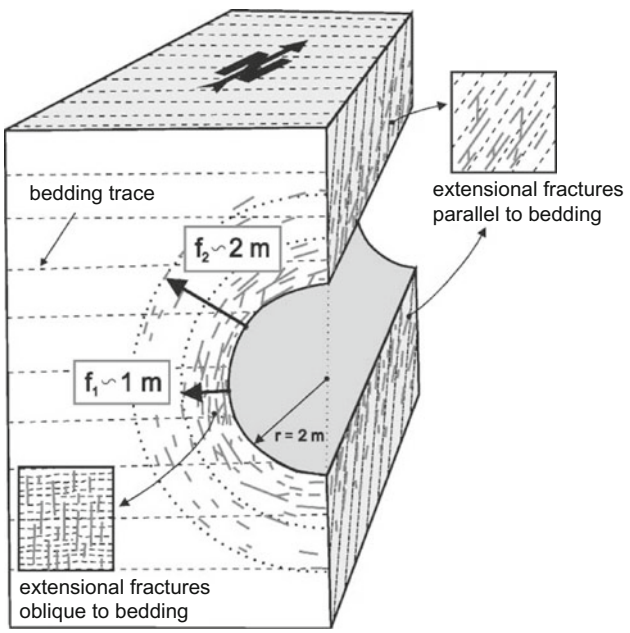

Fig. 15 Conceptual model of the EDZ (after Bossart et al. 2002). The EDZ fracture network related to tunnel excavation can be subdivided into an inner and outer shell. The inner shell, with an average extent of 1 m from the tunnel circumference, is typically characterised by extensional fractures sub-parallel to the tunnel wall and smaller-scale shear fractures. These fractures developed mainly in the tunnel walls (sidewall, ceiling, floor) and tunnel faces. Extensional fractures are often linked by smaller-scale shear fractures, resulting in an interconnected fracture network. The outer shell, between 1 and ca. 2 m from the tunnel circumference, is composed of individual extensional fractures that are not, or only partially, interconnected

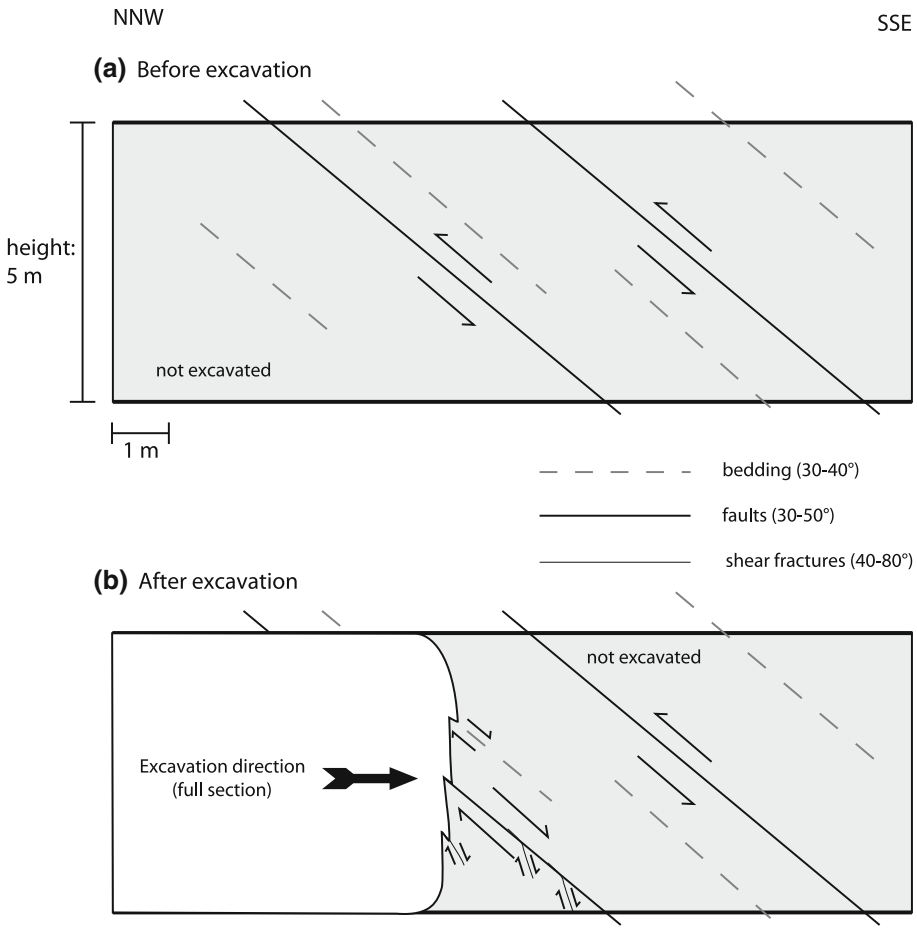

Fig. 16 Geometry and kinematics of EDZ shear fractures identified during the excavation of Gallery 08, which is oriented normal to the bedding strike. **a** Situation prior to excavation. **b** Situation after excavation. Shear fractures induced during tunnel excavation are interpreted as originating from the reactivation of bedding planes and/or sub-parallel pre-existing reverse SSE-dipping faults as normal faults. These induced shear fractures were associated with down-dip striation and sense of shear, indicating normal displacement along the fracture planes

fractures formed as a consequence of stress redistribution already ahead of the tunnel face. Similar findings were made in an underground rock laboratory in the Boom Clay in Belgium (Blümling et al. 2007).

EDZ shear fracture planes were identified in the tunnel faces during the excavation of Gallery 08, which is oriented normal to the bedding strike. These fractures strike parallel to the gallery face and are systematically more inclined than the bedding planes by angles of 20°–40°. They are interpreted as being initiated by the reactivation in normal faulting of bedding planes and/or sub-parallel pre-existing reverse SSE-dipping faults during the excavation phase (Fig. 16). These induced shear fractures were associated with down-dip striation and related kinematics, indicating normal displacement along the fracture planes. Thus, the whole system of pre-existing bedding planes, sub-parallel fault planes and EDZ shear fractures was activated in normal faulting mode. By analogy with larger scale natural fracture zones, the geometry and kinematics of the EDZ shear fractures are similar to strike-slip fault systems and especially to horsetail fractures or branch faults as described in Kim et al. (2004).

5 Conclusions

The Mont Terri rock laboratory is located in the backlimb of a ramp-like anticline, which is characterised by a pronounced along-strike asymmetry resulting from variously oriented inherited faults. At the regional scale the Mont Terri area is significantly affected by N- to NNE-striking normal faults of the Eo-Oligocene Rhine–Bresse graben system and by ENE-striking faults inherited from Late Variscan times. According to their orientation with respect to the transport direction towards the NNW, these faults served as oblique and frontal ramps during the subsequent Jura thrusting and folding in the Late Miocene.

The three different fault systems identified in the rock laboratory clearly correlate with the regional-scale structures. N- and NNE-striking faults segmented the layer-cake structure into distinct blocks. During the propagation of the Alpine foreland front towards the NNW, these inherited faults were reactivated in sinistral strike-slip mode. The detached sediments above the Middle Triassic evaporites may have experienced a slight clockwise rotation as a result of the reactivation of these faults. The S-dipping sub-horizontal faults are interpreted as the subsequent

contraction of the Mont Terri anticline and its slight northward rotation. SSE-dipping faults parallel to the bedding were probably initiated during this late stage of reverse faulting. The SW-dipping faults are interpreted as the result of lateral extension during the thrusting of the Mont Terri anticline above the frontal ramp. The plunge towards the SW is explained by the small rhomb-shaped basin, which replaces the anticline crest. These SW-striking fault planes were reactivated in thrusting mode during the ongoing deformation. Finally, they were folded by the bedding-parallel faults during the later contraction of the Mont Terri anticline. The total shortening consumed by the Mont Terri anticline was estimated by mass (area) balancing to be approximately 2.1 km (Freivogel and Huggenberger 2003).

AMS results provide additional data about the tectonic deformation. A magnetic fabric in the Opalinus Clay developed with a magnetic foliation close to the bedding. In the Opalinus Clay of the backlimb of the Mont Terri anticline, two distinct magnetic lineations were measured. The SW-dipping one is interpreted to be related to the anticlinal folding and the E-W trending one may be related to layer-parallel shortening prior to the folding. Strain imprint is found to be more pronounced in the overturned forelimb, which is consistent with structural data.

As a consequence of tunnel excavation and the associated stress redistribution, fractures are induced on a micro- and macro-scale along the tunnel walls. The EDZ fracture network can be subdivided into an inner and an outer shell. The inner shell, restricted to the first metre of depth in the tunnel wall, typically consists of an interconnected and air-filled fracture network in which extensional fractures are linked by meso-scale shear fractures. The outer shell defines a zone of about 2 m around the tunnel and comprises partially water-saturated and isolated extensional fractures. The three-dimensional distribution of the EDZ fractures in the inner and outer shells is influenced by the pronounced bedding plane anisotropy, especially at the bottom and top of the gallery. In addition, metric EDZ shear-fracture planes can also be identified in the tunnel faces, ceiling and sidewall. According to the interpretation, they resulted from the reactivation of normal faulting of bedding planes and/or sub-parallel and SSE-dipping reverse faulting during the excavation phase. Whatever their orientation, the pre-existing faults spatially limited the propagation of EDZ fractures into the adjacent rock mass. In tunnel sections where only a few pre-existing faults were identified, the majority of EDZ fractures was extensional (Mode I) and the EDZ fracture network was better developed. Also, strike-slip pre-existing small-scale fault and bedding planes are incorporated in the EDZ network. As a consequence of the rock mass heterogeneities (e.g. distribution of pre-existing fractures and fault zones) and their influence on the stress field, the EDZ is heterogeneous in both the mode and possibly the fracturing depth.

Because all the tectonic fault planes are sealed with calcite shear fibres and clay minerals (aligned with the shear direction), the effect of fault-related deformation on the hydraulic and mechanical properties of the clays is very small. This is confirmed by the similarity between the hydraulic conductivity measured in the Main Fault and that derived for the intact matrix ($K = 2 \times 10^{-13}$ m/s). Regarding the EDZ fractures, long-term hydrotesting conducted at various test locations confirmed the self-sealing of these fractures. Fracture transmissivities decrease by two orders of magnitude over a period of 2 years and the trend is still continuing. Whether they are of tectonic origin or induced by tunnel excavation, fractures developed in the Opalinus Clay are either sealed with minerals and/or have self-sealing properties. This observation is of key importance in evaluating the feasibility of deep geological disposal in argillaceous formations.

Acknowledgments We are particularly grateful for the very careful and thoughtful reviews of the manuscript by Kamil Ustaszewski of the University of Potsdam and Peter Huggenberger of the University of Basel. We would like to thank the 14 project partners of the Mont Terri Project for financing the geological documentation. As operator of the underground laboratory, swisstopo, is also thanked for providing the facilities. We are indebted to Thierry Theurillat for his valuable site support during the field mapping in the Mont Terri laboratory. We would also like to thank Gilles Armand, Tim Vietor and Kristof Schuster for the fruitful discussions during our field work in the laboratory. Linda McKinley is gratefully acknowledged for improving the English of the manuscript and Peter Müller for the careful improvement of the figures.

References

Affolter, T., & Gratier, J.-P. (2004). Map view retrodeformation of an arcuate fold-and-thrust belt: The Jura case. *Journal of Geophysical Research, 109*, B03404. doi:10.1029/2002JB002270.

Allia, V. (1996). Sedimentologie und Ablagerungsgeschichte des Opalinustons in der Nordschweiz. *Ph.D. dissertation*, Geologisch-Paläontologisches Institut, University of Basel, Nr. 10, 1996.

Aubourg, C., Pozzi, J.-P., Janots, D., & Sahraoui, L. (2008). Imprinting chemical remanent magnetization in claystones at 95°C. *Earth and Planetary Science Letters, 272*, 172–180.

Aubourg, C., Smith, B., Bakhtari, H., Guya, N., Eshraghi, A., Lallemant, S., et al. (2004). Post-Miocene shortening pictured by magnetic fabric across the Zagros-Makran syntaxis. In A. J. Sussman & A. B. Weil (Eds.), *Orogenic curvature: Integrating paleomagnetic and structural analyses* (pp. 17–40). Boulder, CO: Geological Society of America.

Bahat, D. (1986). Criteria for the differentiation of en-echelons and hackles in fractured rocks. *Tectonophysics, 121*, 197–206.

Baer, M., Deichmann, N., Braunmiller, J., Husen, S., Faeh, D., Giardini, D., Kaestli, Ph., Kradolfer, U., & Wiemer, S. (2005). Earthquakes in Switzerland and surrounding regions during 2004. *Eclogae Geologicae Helvetiae, 98*, 407–418. doi:10.1007/s00015-005-1168-3.

Becker, A. (2000). The Jura Mountains: An active foreland fold-and-thrust belt? *Tectonophysics, 321*, 381–406.

Berger, J.-P. (1996). Cartes paléogéographiques-palinspatiques du bassin molassique suisse (Oligocène inférieur-Miocène moyen). *Neues Jahrbuch für Geologie und Paläontologie—Abhandlungen, 202/1*, 1–44.

Bergerat, F. (1977). Le rôle des décrochements dans les liaisons tectoniques entre le fossé de la Saône et le fossé rhénan. *Compte Rendu de la Société Géologique de France, 4*, 195–199.

Bergerat, F. (1987). Paléo-champs de contrainte tertiaires dans la plate-forme européenne au front de l'orogène alpin. *Bulletin de la Société géologique de France, 8/3*, 611–620.

Blaesi, H.-R. (1987). Lithostratigraphie und Korrelation der Doggersedimente in den Bohrungen Weiach, Riniken und Schafisheim. *Eclogae Geologicae Helvetiae, 80*, 415–430.

Blaesi, H.-R., Peters, T. J., & Mazurek, M. (1991). Der Opalinuston des Mont Terri (Kanton Jura). Lithologie, Mineralogie und physiko-chemische Gesteinsparameter. NAGRA internal Report.

Blümling, P., Bernier, F., Lebon, P., & Martin, C. D. (2007). The excavation damaged zone in clay formations: Time-dependent behaviour and influence on performance assessment. *Physics and Chemistry of the Earth, 32*, 588–599.

Bolliger, T., Engesser, B., & Weidmann, M. (1993). Première découverte de mammifères pliocènes dans le Jura neuchâtelois. *Eclogae Geologicae Helvetiae, 86*, 1031–1068.

Borradaile, G. (1988). Magnetic susceptibility, petrofabric and strain—a review. *Tectonophysics, 156*, 1–20.

Borradaile, G. J., & Jackson, M. (2004). Anisotropy of magnetic susceptibility (AMS): Magnetic petrofabric of deformed rocks. In F. Martín-Hernández, C. M. Lüneburg, C. Aubourg, & M. Jackson (Eds.), *Magnetic fabric, methods and applications* (Vol. 238, pp. 299–360) London: Geological Society Special Publications.

Borradaile, G. J., & Mothersill, J. S. (1984). Coaxial deformed and magnetic fabrics without simply correlated magnitudes of principal values. *Physics of the Earth and Planetary Interiors, 35*, 294–300.

Bossart, P., Meier, P., Möri, A., Trick, Th., & Mayor, J. C. (2002). Geological and hydraulic characterisation of the excavation disturbed zone in the Opalinus Clay of the Mont Terri Rock Laboratory. *Engineering Geology, 66*, 19–38.

Bossart, P., & Thury, M. (2008). *Mont Terri Rock Laboratory. Project, programme 1996 to 2007 and results*. Wabern: Reports of the Swiss Geological Survey no. 3.

Bossart, P., Trick, Th., Meier, P. M., & Mayor, J. C. (2004). Structural and hydrogeological characterisation of the excavation-disturbed zone in the Opalinus Clay (Mont Terri Project, Switzerland). *Applied Clay Science, 26*, 429–448.

Buechi, U. P. (1965). Geologische Ergebnisse der Erdölexploration auf das Mesozoikum im Untergrund des schweizerischen Molassebecken. *Bulletin der schweizerischen Vereinigung Petroleum-Geologen und -Ingenieure, 32*, 7–38.

Burkhalter, R. M. (1996). Die Passwang-Alloformation (unteres Aalenien bis unteres Bajocien) im zentralen und nördlichen Schweizer Jura. *Eclogae Geologicae Helvetiae, 89*, 875–934.

Burkhalter, R. M., Blaesi, H.-R., & Feist-Burkhardt, S. (1997). Der "Dogger β" (oberes Aalénien) in den Bohrungen Herdern-1, Berlingen-1 und Kreuzlingen-1 (Nordostschweiz) und seine Beziehung zu den gleichaltrigen Schichten im Nordjura. *Eclogae Geologicae Helvetiae, 90*, 269–292.

Burkhard, M. (1990). Aspects of the large scale Miocene deformation in the most external part of the Swiss Alps (Subalpine Molasse to Jura fold belt). *Eclogae Geologicae Helvetiae, 83*, 559–583.

Burkhard, M., & Sommaruga, A. (1998). Evolution of the western Swiss Molasse basin: structural relations with the Alps and the Jura belt. In A. Mascle, C. Puigdefàbregas, H. P. Luterbacher, & M. Fernàndez (Eds.), *Cenozoic foreland basins of Western Europe* (pp. 279–298). Geological Society Special Publications 134.

Buxtorf, A. (1907). Zur Tektonik des Kettenjura. *Ber. Vers. Oberr. Geol. Vers.*, *30/40*, 79–111.

Constable, C., & Tauxe, L. (1990). The bootstrap for magnetic susceptibility tensors. *Journal of Geophysical Research, 95*(B6), 8383–8395.

Duringer, P. (1988). Les conglomérats des bordures du rift cénozoïque rhénan. Dynamique sédimentaire et contrôle climatique. *Ph.D. dissertation*, Université Louis Pasteur, Strasbourg, France.

Favre, J., Bourquin, P., & Stehlin, H. G. (1937). Etudes sur le Tertiaire du Haut-Jura neuchâtelois. *Mémoire de la Société de Paléontologie, Suisse, 60*, 1–47.

Freivogel, M., & Huggenberger, P. (2003). Modellierung bilanzierter Profile im Gebiet Mont Terri—La Croix (Kanton Jura). In P. Heitzmann & J.-P. Tripet (Eds.), *Mont Terri Project—geology, paleohydrology and stress field of the Mont Terri region*. Bern: Rapports de l'OFEG, Série Géologie, No. 4.

Frizon de Lamotte, D., Souque, C., Grelaud, S., & Robion, P. (2002). Early record of tectonic magnetic fabric during inversion of a sedimentary basin. Short review and examples from the Corbières transfer zone (France). *Bulletin de la Société Géologique de France, 173*, 461–469.

Gehrig, A. U., Keller, P., & Heller, F. (1991). Paleomagnetism and tectonics of the Jura arcuate mountain belt in France and Switzerland. *Tectonophysics, 186*, 269–278.

Giamboni, M., Ustaszewski, K., Schmid, S. M., Schumacher, M. E., & Wetzel, A. (2004). Plio-Pleistocene transpressional reactivation of Paleozoic and Paleogene structures in the Rhine-Bresse transform zone (northern Switzerland and eastern France). *International Journal of Earth Science, 93*, 207–223.

Heim, A. (1919). *Geologie der Schweiz*. Leipzig: Tauchnitz.

Hirt, A. M., Lowrie, W., Clendenen, W. S., & Kligfield, R. (1988). The correlation of magnetic anisotropy with strain in the Chelmsford Formation of the Sudbury Basin, Ontario. *Tectonophysics, 145*, 177–189.

Homberg, C., Angelier, J., Bergerat, F., & Lacombe, O. (1994). Nouvelles données tectoniques dans le Jura externe: apport des paléocontraintes. *Compte rendu de l'Académie des Sciences (Paris) Série II, 318/10*, 1371–1377.

Hrouda, F. (1982). Magnetic anisotropy of rocks and its application in geology and geophysics. *Geophysical Surveys, 5*, 37–82.

Jordan, P. (1994). Evaporite als Abscherhorizonte. *Beitrag Geologische Karte Schweiz, 164*, 1–79.

Kälin, D. (1993). Stratigraphie und Säugetierfaunen der obersten Süsswassermolasse des Nordwestschweiz. *Ph.D. dissertation*, ETH Zürich, Zürich, Switzerland.

Kastrup, U., Zoback, M. L., Deichmann, N., Evans, K. F., Giardini, D., & Michael, A. J. (2004). Stress field variations in the Swiss Alps and the northern Alpine foreland derived from inversion of fault plane solutions. *Journal of Geophysical Research, 109*. doi: 10.1029/2003JB002550.

Kim, Y.-S., Peacock, D. C. P., & Sanderson, D. J. (2004). Fault damage zones. *Journal of Structural Geology, 26*, 503–517.

Lacombe, O., Angelier, J., Byrne, D., & Dupin, J. (1993). Eocene-Oligocene tectonics and kinematics of the Rhine-Saone continental transform zone (Eastern France). *Tectonics, 12*, 874–888.

Laubscher, H. P. (1961). Die Fernschubhypothese der Jurafaltung. *Eclogae Geologicae Helvetiae, 54*, 221–280.

Laubscher, H. P. (1963). *Erläuterungen zum Geologischen Atlasblatt "1085 St-Ursanne, 1:25'000"*. Basel: Schweizerische Geologische Kommission.

Laubscher, H. P. (1965). Ein kinematisches Modell der Jurafaltung. *Eclogae Geologicae Helvetiae, 58*, 231–318.

Laubscher, H. P. (1970). Grundsätzliches zur Tektonik des Rheingrabens. In J. H. Illies & S. Mueller (Eds.), *Graben problems.*

Proceedings of an international Rift symposium held in Karlsruhe 1968, International Upper Mantle Project (pp. 79–86). Stuttgart: E. Schweizerbart.

Laubscher, H. P. (1972). Some overall aspects of Jura dynamics. *American Journal of Science, 272*, 293–304.

Laubscher, H. P. (1987). Die tektonische Entwicklung der Nordschweiz. *Eclogae Geologicae Helvetiae, 80*, 287–303.

Laubscher, H. P. (2001). Plate interactions at the southern end of the Rhine Graben. *Tectonophysics, 343*, 1–19.

Madritsch, H., Preusser, F., Fabbri, O., Bichet, V., Schlunegger, F., & Schmid, S. M. (2010). Late Quaternary folding in the Jura Mountains: Evidence from syn-erosional deformation of fluvial meanders. *Terra Nova, 22*, 147–154. doi:10.1111/j.1365.3121.2010.00928.

Madritsch, H., Schmid, S. M., & Fabbri, O. (2008). Interactions between thin-and thick-skinned tectonics at the northwestern front of the Jura fold-and-thrust belt (eastern France). *Tectonics, 27*, TC5005. doi:10.1029/2008TC002282.

Mazurek, M., Hurford, A., & Leu, W. (2006). Unravelling the multistage burial history of the Swiss Molasse Basin: Integration of apatite fission track, vitrinite reflectance and biomarker isomerisation analysis. *Basin Research, 18*, 27–50.

Mosar, J. (1999). Present-day and future tectonic underplating in the western Swiss Alps: Reconciliation of basement/wrench-faulting and décollement folding of the Jura and Molasse basin in the Alpine foreland. *Earth and Planetary Science Letters, 173/3*, 143–155.

Müller, W. H., Huber, M., Isler, A., & Kleboth, P. (1984). *Erläuterungen zur geologischen Karte der zentralen Nordschweiz. 1:1000'000*. NAGRA Technischer Bericht 84-25 and SGG, Geol. Spez. Karte 121, pp. 1–234.

Nussbaum, C., & Bossart, P. (2008). Geology. In P. Bossart & M. Thury (Eds.), *Mont Terri Rock Laboratory. Project, programme 1996 to 2007 and results*. Wabern: Reports of the Swiss Geological Survey no. 3.

Passchier, C. W., & Trouw, R. A. J. (1996). *Microtectonics*. Berlin: Springer.

Philippe, Y., Colleta, B., Devill, E., & Mascle, A. (1996). The Jura fold-and-thrust belt: A kinematics model based on map balancing. In P. Ziegler & F. Horvath (Eds.), *Peri-Tethys Memoir 2: Structure and prospects of Alpine basins and forelands* (Vol. 170, pp. 235–261) Paris: Mémoire du Muséum National d'Histoire Naturelle.

Picot, L., Becker, D., Lapaire, F., Ustaszewski, K., Hug, W. A., & Berger, J. P. (2005). Sédimentologie, paléontologie et paléoenvironnements côtiers de la région de Porrentruy (Sud-Rhénan, Paléogène, Jura, Suisse): Implications géodynamiques. *Eclogae Geologicae Helvetiae, 98*, 281–296. doi:10.1007/s00015.005.1154.9.

Plessmann, W. (1972). Horizontal-Stylolithen im Französisch-schweizerischen Tafel- und Faltenjura und ihre Einpassung in den regionalen Rahmen. *Geologische Rundschau, 61*, 332–347.

Ramsay, J. G., & Huber, M. I. (1983). *The techniques of modern structural geology, 1: Strain analysis*. London: Academic Press.

Robion, P., Grelaud, S., & Frizon de Lamotte, D. (2007). Pre-folding magnetic fabrics in fold-and-thrust belts: Why the apparent internal deformation of the sedimentary rocks from the Minervois basin (NE—Pyrenees, France) is so high compared to the Potwar basin (SW—Himalaya, Pakistan)? *Sedimentary Geology, 196*, 181–200.

Rochette, P., Jackson, J., & Aubourg, C. (1992). Rock magnetism and the interpretation of anisotropy of magnetic susceptibility. *Review of Geophysics, 30*, 209–226.

Schaeren, G., & Norbert, J. (1989). Tunnels du Mont Terri et du Mont Russelin. La Traversée des "Roches à Risques": Marnes et Marnes à Anhydrite. *Société suisse des ingénieurs et des architectes*, Documentation, SIA D 037, Zürich, pp. 19–24.

Sommaruga, A. (1997). Tectonics of the Central Jura and the Molasse Basin: New insights from the interpretation of seismic reflection data. *Mémoire de la Société Neuchâteloise des Sciences Naturelles, 12*, 145.

Sommaruga, A. (1999). Décollement tectonics in the Jura foreland fold-and-thrust belt. *Marine and Petroleum Geology, 16*, 11–134.

Suppe, J. (1983). Geometry and kinematics of fault-bend folding. *American Journal of Science, 283*, 684–721.

Suppe, J., Connors, C. D., & Zhang, Y. (2004). Shear fault-bend folding. In K. McClay (Ed.), *Thrust tectonics and hydrocarbon systems* (pp. 303–323). Tulsa: American Association of Petroleum Geologists.

Suppe, J., & Medwedeff, D. A. (1990). Geometry and kinematics of fault-propagation folding. *Eclogae Geologicae Helvetiae, 83*, 409–459.

Suter, M. (1981). Strukturelles Querprofil durch den nordwestlichen Faltenjura, Mt-terri-Randüberschiebung-Freiberge. *Eclogae Geologicae Helvetiae, 74*, 255–275.

Thomas, W. A. (1990). Controls on locations of transverse zones in thrust belts. *Eclogae Geologicae Helvetiae, 83*, 645–664.

Thury, M., & Bossart, P. (1999). *Results of the hydrogeological, geochemical and geotechnical experiments performed in the Opalinus Clay (1996–1997)*. Bern-Ittigen: Geological report no. 23, Swiss Geological Survey.

Tschanz, X. (1990). Analyse de la déformation du Jura central entre Neuchâtel (Suisse) et Besançon (France). *Eclogae Geologicae Helvetiae, 83*, 543–588.

Tschanz, X., & Sommaruga, A. (1993). Deformation associated with folding above frontal and oblique ramps around the rhomb shaped Val-de-Ruz basin (Jura Mountains). *Annales Tectonicae, 7*, 53–70.

Ustaszewski, K., & Schmid, S. M. (2006). Control of preexisting faults on geometry and kinematics in the northernmost part of the Jura fold-and-thrust belt. *Tectonics, 25*, TC5003.

Ustaszewski, K., & Schmid, S. M. (2007). Latest Pliocene to recent thick-skinned tectonics at the Upper Rhine Graben–Jura Mountains junction. *Swiss Journal of Geosciences, 100*, 293–312.

Ustaszewski, K., Schumacher, M. E., & Schmid, S. M. (2005). Simultaneous normal faulting and extensional flexuring during rifting: an example from the southernmost Upper Rhine Graben. *International Journal of Earth Sciences, 94*, 680–696. doi:10.1007/s00531-004-0454-z.

Valley, B., Burkhard, M., & Schnegg, P. A. (2004). Dépliage 3-D des anticlinaux bordant le synclinal fermé de la vallée des Ponts, Jura central, Suisse. *Eclogae Geologicae Helvetiae, 97*, 279–291.

Valley, B., & Evans, K. F. (2009). Stress orientation to 5 km depth in the basement below Basel (Switzerland) from borehole failure analysis. *Swiss Journal of Geosciences, 102*, 467–480.

Yong, S. (2007). A three-dimensional analysis of excavation-induced perturbations in the Opalinus Clay at the Mont Terri Rock Laboratory. *Ph.D. dissertation*, Geological Institute, ETH Zürich, Switzerland.

Yong, S., Kaiser, P. K., & Loew, S. (2010). Influence of tectonic shears on tunnel-induced fracturing. *International Journal of Rock Mechanics & Mining Sciences, 47*, 894–907.

Ziegler, P. A. (1992). European Cenozoic rift system. *Tectonophysics, 208*, 91–111. doi:10.1016/0040.1951(86)90236.2.